Tracking the Nearfield Evolution of an Initially Shallow, Neutrally Buoyant Plane Jet Over a Sloping Bottom Boundary

H. Shi, Maria Eletta Negretti, Julien Chauchat, K. Blanckaert, U. Lemmin, D A Barry

AGU ADVANCING EARTH AND SPACE SCIENCES

Water Resources Research

RESEARCH ARTICLE
10.1029/2023WR034826

Tracking the Nearfield Evolution of an Initially Shallow, Neutrally Buoyant Plane Jet Over a Sloping Bottom Boundary

H. Shi[1,2], M. E. Negretti[3], J. Chauchat[3], K. Blanckaert[4], U. Lemmin[1], and D. A. Barry[1]

[1]Ecological Engineering Laboratory (ECOL), Faculty of Architecture, Civil and Environmental Engineering (ENAC), Environmental Engineering Institute (IIE), École Polytechnique Fédérale de Lausanne (EPFL), Lausanne, Switzerland, [2]Now at School of Ocean Sciences, Bangor University, Menai Bridge, Anglesey, UK, [3]Université Grenoble Alpes, CNRS, Grenoble INP, LEGI UMR 5519, Grenoble, France, [4]Research Unit Hydraulic Engineering and Environmental Hydromechanics, Institute of Hydraulic Engineering and Water Resources Management, Technische Universität Wien, Vienna, Austria

Key Points:

- Combined physical/numerical experiments allowed the first characterization of a neutrally buoyant plane jet over a sloping bottom
- Sloping bottom jets converge laterally near the mouth and have narrower, shorter flow establishment zones than horizontal bottom jets
- Coherent structures developing in the shear layers contribute significantly to turbulent kinetic energy production and momentum exchange

Supporting Information:

Supporting Information may be found in the online version of this article.

Correspondence to:

H. Shi,
haoran.shi@epfl.ch;
h.shi@bangor.ac.uk

Citation:

Shi, H., Negretti, M. E., Chauchat, J., Blanckaert, K., Lemmin, U., & Barry, D. A. (2024). Tracking the nearfield evolution of an initially shallow, neutrally buoyant plane jet over a sloping bottom boundary. *Water Resources Research*, *60*, e2023WR034826. https://doi.org/10.1029/2023WR034826

Received 5 MAR 2023
Accepted 9 APR 2024

Author Contributions:

Conceptualization: K. Blanckaert
Data curation: H. Shi, M. E. Negretti
Formal analysis: H. Shi, M. E. Negretti
Funding acquisition: D. A. Barry
Investigation: H. Shi
Methodology: H. Shi, M. E. Negretti
Software: J. Chauchat
Supervision: M. E. Negretti, J. Chauchat, K. Blanckaert, U. Lemmin, D. A. Barry
Validation: H. Shi
Writing – original draft: H. Shi
Writing – review & editing: M. E. Negretti, J. Chauchat, K. Blanckaert, U. Lemmin, D. A. Barry

Abstract Understanding coastal plane jets which occur when a body of water discharges into an ocean or a lake through a channel or outlet is important, since they play a significant role in sediment, nutrient, and pollutant exchange. This study investigates the nearfield of initially shallow, neutrally buoyant plane jets, bounded by a free surface and a sloping bottom (Sloping Bottom Jet; SBJ) that issue into a laterally unconfined quiescent ambient both experimentally and numerically, and compares them with a plane jet flowing over a horizontal bottom (Horizontal Bottom Jet; HBJ). Results revealed that, different from the HBJ, the width and centerline velocity of SBJ decrease near the mouth. The SBJ width gradually increases after that as the transverse longitudinal velocity profile progressively transforms from a "top-hat" into a Gaussian distribution. Once the Gaussian distribution is established, both jets diverge and centerline velocity decreases. Shear layers are generated on the sides of both jets with Kelvin Helmholtz-type Coherent Structures (KHCS) developing inside. KHCS produce periodic velocity fluctuations with a Strouhal number of ∼0.079 and contribute significantly to momentum exchange and turbulent kinetic energy production. Since the thickness of the SBJ increases longitudinally, the vertical extent of KHCS also increases. When the two shear layers meet and merge at the centerline, they cause a flapping motion of the jet. This location is closer to the jet mouth for SBJs than for the HBJ. These findings demonstrate that a sloping bottom modifies the flow field from quasi-2D for the HBJ to strongly 3D for SBJs.

1. Introduction

Discharge of a body of water into an ocean or a lake through a channel or an outlet that resembles a neutrally buoyant flow into a quiescent ambient is a common feature of coastal environments. Understanding the development of this exchange flow, particularly in the nearfield of an outlet, is important since the jet-like discharge plays a significant role in the exchange of sediments, nutrients, and pollutants from rivers, bays or harbors to oceans or lakes. This is crucial with respect to the biogeochemical evolution of marine and lacustrine ecosystems in the coastal environment (Bianchi & Allison, 2009; Brown et al., 2000; McKee et al., 2004; Yao et al., 2016). Being able to characterize this flow allows optimally managing the coastal environment on a large scale. This exchange flow is often complex. However, much can be learned about its hydrodynamics when it is approximated by a shallow plane-jet flowing into a quiescent ambient (Cohen, 2012; Ortega-Sánchez et al., 2008; Özsoy & Ünlüata, 1982; Rowland et al., 2009). Previous investigations of neutrally buoyant plane jets bounded by a solid flat-bottom boundary and an upper free surface issuing from a wide, rectangular cross-section opening into a quiescent ambient, simulated aspects of the exchange flow from an outlet into the coastal environment (Cohen, 2012; Jiménez-Robles et al., 2016; Ortega-Sánchez et al., 2008; Rowland et al., 2009). The hydrodynamics of this configuration (Figures 1a and 1b) will be investigated in the present study in the laboratory and by numerical methods in order to provide insight into the characteristics of the exchange flow; this may also serve as a guide for field studies in the coastal environment that are often difficult to carry out.

In previous laboratory studies, plane jets were bounded by parallel horizontal boundaries (free surface and/or solid horizontal wall(s); Cohen, 2012; Deo et al., 2007, 2008; Dracos et al., 1992; Giger et al., 1991; Jirka, 2001; Rowland et al., 2009). Assuming homogeneity in the vertical direction, the jet could be treated as quasi two-

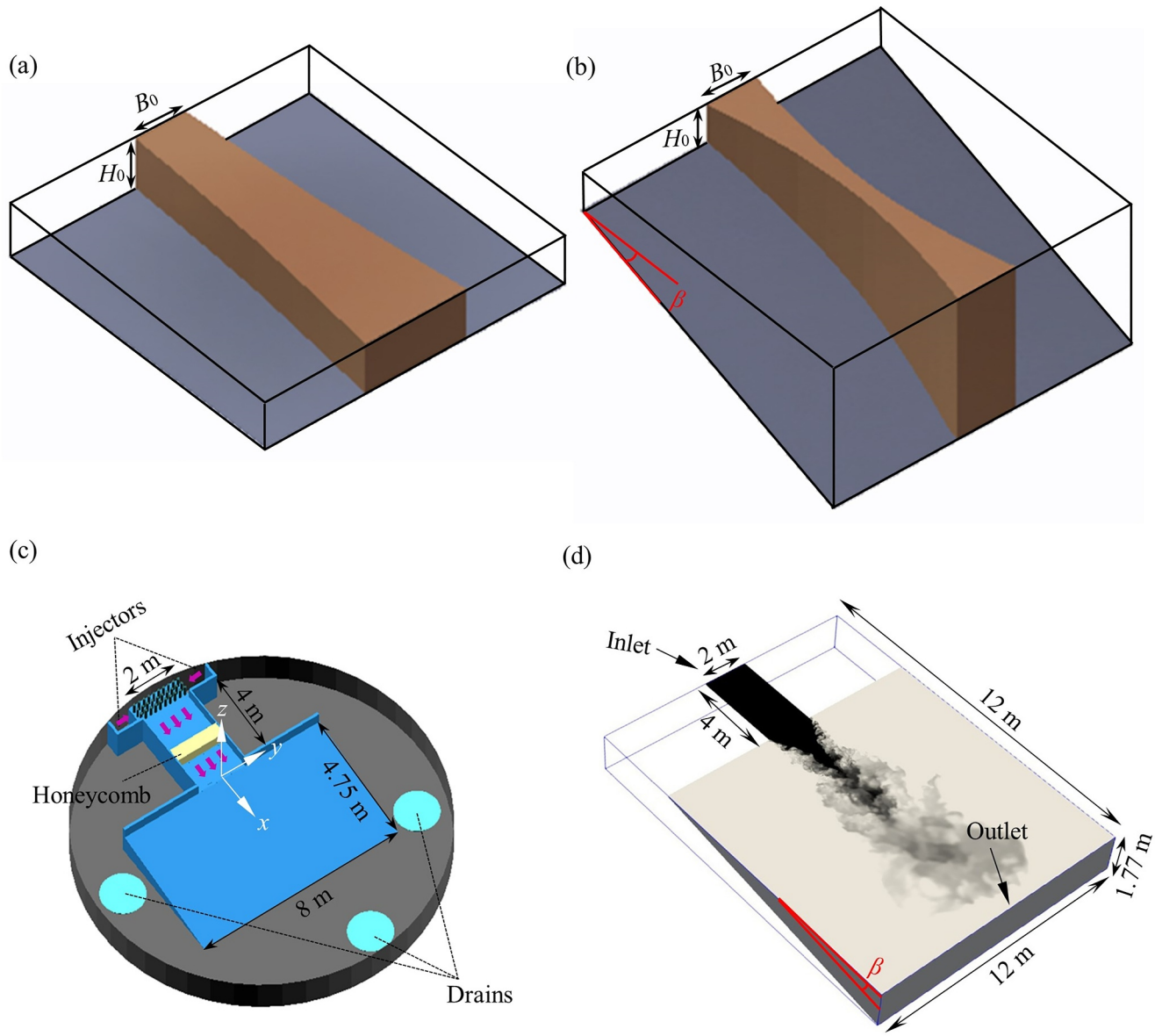

Figure 1. Three-dimensional (3D) depth-exaggerated sketch of a neutrally buoyant plane jet flowing over: (a) a horizontal bottom and (b) a sloping bottom. (c) Experimental setup inside the Coriolis Platform. The jet flow was generated in a 4-m long free-surface inlet channel, which entered the wide ambient water body with an 8° sloping bottom. The white arrows indicate the coordinate system. Its origin is in the center at the surface end of the inflow channel. (d) 3D sketch of the simplified geometry used in the numerical model. The jet is colored in black, and the ambient water in gray.

dimensional (2D). The jet mean flow is longitudinal, and ambient fluid is entrained on both sides resulting in an increase of the jet width (Figure 1a). Shear layers develop on both sides of the jet, generating Kelvin Helmholtz-type Coherent Structures (KHCS) with vertical axes. The transverse profile of the longitudinal jet velocity gradually transforms from a "top-hat" profile in the flow establishment zone into a Gaussian profile in the established flow zone (Pope, 2000). Thereafter, the jet becomes self-similar and the centerline velocity starts to decrease (Cohen, 2012; Deo et al., 2007; Heskestad, 1965; Pope, 2000; Rowland et al., 2009). At the location where the Gaussian profile is reached, the shear layers at the two sides of the jet join at the centerline and can cause the jet to meander, a phenomenon known as "jet flapping" (Cohen, 2012; Deo et al., 2007; Dracos et al., 1992; Landel et al., 2012; Thomas & Goldschmidt, 1986). Analytical solutions for the main characteristics of quasi-2D plane jets (i.e., width, centerline velocity, transverse velocity profile, turbulent viscosity) that predict their variations in the longitudinal direction are available (Cohen, 2012; Deo et al., 2007; Heskestad, 1965; Pope, 2000; Rowland et al., 2009).

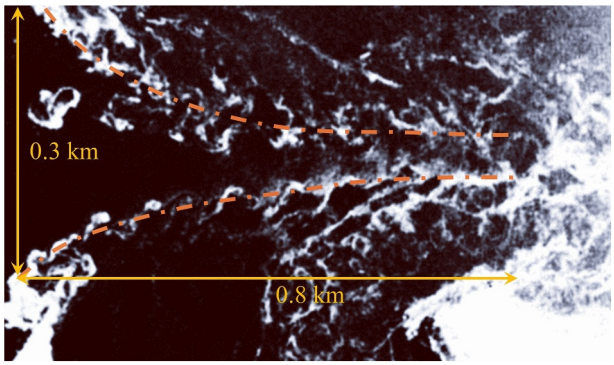

Figure 2. Ebb jet flow through Naruto Strait (Japan; aerial photograph modified after Onishi (1984) with permission from the publisher Elsevier). Note the contraction of the jet (highlighted by orange dash-dotted lines) and the formation of Kelvin-Helmholtz vortices at both sides of the jet. Arrows: outlet width and the length of the flow establishment zone. Flow is from left to right; bottom slope of the ambient: $\beta \approx 2°$.

However, jets over a sloping bottom in coastal environments behave different from the horizontal bottom plane jets discussed above (Broekema et al., 2018; Jiménez-Robles et al., 2016; Ortega-Sánchez et al., 2008) since they gradually spread in the vertical direction (Figure 1b). Analytical models describing the development of jets flowing over sloping boundaries were established by Özsoy and Ünlüata (1982) and Ortega-Sánchez et al. (2008). Ortega-Sánchez et al. (2008) suggested that, unlike horizontal bottom plane jets, sloping bottom jets first undergo a horizontal contraction as a result of their vertical extension, before spreading laterally due to entrainment. A typical example of such a flow in the coastal environment is the ebb jet flowing through Naruto Strait in Japan (Figure 2).

In contrast to extensively investigated horizontal bottom plane jets, laboratory studies of initially shallow plane jets (initial aspect ratio: $B_0/H_0 > 5$) flowing over a sloping bottom have yet to be reported, and validated numerical and analytical models for such a configuration are not available. Here, B_0 and H_0 denote the initial width and depth of the jet, respectively. In this study, we conducted the first combined investigation of laboratory experiments and numerical modeling of an initially shallow, free-surface neutrally buoyant plane jet flowing from a horizontal rectangular channel onto a sloping solid bottom (8°) boundary in an unconfined ambient. Certain findings are compared with those obtained from a numerical, horizontal bottom plane jet study with the same flow configuration. After validation, the numerical model was also applied to different slopes ($0° < \beta < 8°$), since globally, 85% of nearshore slopes in oceans are reported to be <8° (Athanasiou et al., 2019). The following questions are addressed:

- What are the similarities and differences between a neutrally buoyant plane jet flowing over a sloping bottom and a quasi-2D plane jet flowing over a horizontal bottom in terms of mean flow development?
- Can the features of a neutrally buoyant plane jet flowing over a sloping bottom, suggested by existing analytical models, be verified by our experiments and numerical modeling results? If not, what are the limitations of the analytical models?
- Are the characteristics of the shear layers and Kelvin Helmholtz-type Coherent Structures (KHCS) affected by the bottom slope?
- What contributions do KHCS make to the momentum exchange across the jet-ambient interface and the production of turbulent kinetic energy?

The Supporting Information (SI) provides texts and figures (with prefix S) with additional details and clarifications of certain topics discussed in the main text.

2. Materials and Methods

2.1. Laboratory Experiments

The laboratory experiments were conducted in the 1.2-m deep circular tank (diameter 13 m) of the LEGI Coriolis Platform (Université Grenoble Alpes, CNRS, Grenoble, France) (Figure 1c). The same experimental set-up and measurement techniques were used as in Shi et al. (2022), who investigated negatively buoyant plumes. Water was discharged from a horizontal 2-m wide (B_0), 4-m long and 0.08-m deep (H_0), straight inflow channel into an unconfined ambient (8-m wide × 4.75-m long) with an inclined bottom boundary (8° slope). The water depth was kept constant during the experiment (0.08 m in the inflow channel and 0.75 m in the circular tank) by extracting water at the same volume flux as the inflow (Q_0) through three outlet drains positioned at the sides and below the sloping boundary on the tank floor (Figure 1c; for more details, see Text S1 in Supporting Information S1).

The instantaneous velocity field in the horizontal plane at $z/H_0 = -0.5$ with a spatial resolution of ~0.01 m × 0.01 m was obtained from Particle Image Velocimetry (PIV) measurements. The measurement error for the instantaneous velocities was estimated to be ~3% (details in Text S1 of the Supporting Information S1). A Cartesian coordinate system (x: longitudinal, y: transversal, z: vertical) is applied (Figure 1c); its origin (0, 0, 0) is located at the water surface and at the centerline at the downstream end of the inlet channel. Velocities in the x, y and z directions are

Table 1
Summary of Parameters Used in Experimental (EXP) and Numerical (NUM) Cases

	Case	Q_0 (L s^{-1})	U_0 (m s^{-1})	Fr_0	Re_0	β (°)
EXP & NUM	1	18	0.115	0.13	9,000	8
	2	12	0.075	0.08	6,000	8
NUM only	rf	18	0.115	0.13	9,000	0
	3	18	0.115	0.13	9,000	1
	4	18	0.115	0.13	9,000	2
	5	18	0.115	0.13	9,000	4

$u = \overline{u} + u'$, $v = \overline{v} + v'$, and $w = \overline{w} + w'$, respectively; the overbar denotes time-averaged values and the prime, velocity fluctuations.

Two cases (hereinafter referred to as Case 1 and Case 2) with different inflow velocities (Table 1) were investigated resulting in two different inflow Froude numbers ($Fr_0 = U_0/\sqrt{gH_0}$ equal to 0.08 for Case 1 and 0.13 for Case 2), which are within the range of Froude numbers (0.08–0.18) reported in the literature for tidal ebb jets (Broekema et al., 2018; Cohen, 2012; Onishi, 1984). Here, U_0 is the bulk average velocity of the jet at the channel mouth and g is the magnitude of gravitational acceleration.

2.2. Numerical Model

To simulate the experiments, a three-dimensional (3D) numerical model using Large Eddy Simulation (LES) based on the open-source CFD package OpenFOAM (De Lorenzis & Düster, 2020; Jasak, 2009; Weller et al., 1998) was adapted using the validated model configuration of Shi et al. (2022). A simplified geometry consisting of a rectangular inlet channel connected to a receiving tank with an 8° sloping bottom (Figure 1d) was applied to represent the geometry of the laboratory experiment. Two different inflow configurations for the jet over the sloping bottom were investigated (Cases 1 and 2 in Table 1). For more details of the model configuration, see Text S2 in Supporting Information S1. Text S3 in Supporting Information S1 gives further verification and validation of the model including a grid convergence index analysis and a comparison with experimental data for a shallow plane jet flowing over a horizontal bottom reported by Cohen (2012). The numerical model provided 3D flow field data at different depths, and also extended the range of the investigated domain in the offshore direction, beyond that of the experimental investigations. The model was also applied for other bottom slopes, $\beta = 0°, 1°, 2°, 4°$ (Table 1). Case rf ($\beta = 0°$) was used as a reference case to determine the similarities and differences between sloping bottom and horizontal bottom jets.

3. Results and Discussion

3.1. Mean Flow Characteristics and Their Comparison With Theories

Time-averaged quantities are similar for the two 8° sloping bottom cases. Therefore, the focus will mainly be on Case 1 and the comparison with horizontal bottom Case rf. The measured mean velocity field at $z/H_0 = -0.5$ shows that, in contrast to the classical quasi-2D horizontal bottom plane jet, the jet in Case 1 converges laterally near the channel mouth (Figure 3a). This agrees with the outlet discharge observed in the coastal environment (e.g., Figure 2). The longitudinal velocity profile along the centerline ($y = 0$) drops steeply until $x/B_0 = 0.5$ (Figure 3b). It then slightly increases and decreases again before reaching $x/B_0 = 1.6$ (Figure 3b). The transverse velocity distributions at $x/B_0 = 0.4$ and 0.8 present a "top-hat" profile with a central region of laterally uniform longitudinal velocity (Figure 3c). The velocity profile gradually transforms. At $x/B_0 = 1.2$, the "top-hat" region becomes much smaller and then disappears in the established flow zone at $x/B_0 = 1.6$, at the limit of the measured domain. The half width of the "top-hat" region (r) gradually decreases from $0.5B_0$ at the channel mouth to zero at $x/B_0 = 1.6$.

Different from Case 1, the jet in Case rf spreads laterally from the channel mouth (Figure 4a). With increasing offshore distance, a bottom boundary layer gradually develops (Figure 4b, velocity distribution in the central section, $y/B_0 = 0$). For sloping bottom Case 1, the numerical velocity distribution at $z/H_0 = -0.5$ (Figure 4c) is very similar to that observed in the experiment (Figure 3a). Beyond $x/B_0 > 1.6$, the jet starts to diverge.

The velocity field was obtained in an inclined plane that was parallel to the sloping bottom boundary and was 2 cm above it (Figure 4d). The velocity field features a region of low velocity inside the jet (dashed-lined triangle), resulting from the angle between the inflow velocity and the sloping bottom. A similar low velocity region at that location was also observed by Shi et al. (2022) for negatively buoyant plumes over a sloping bottom boundary. The depth-averaged velocity distribution for Case 1 (Figure 4e) is similar to the one close to the water surface (Figure 4c) but has a smaller magnitude. Unlike Case rf, the jet in Case 1 spreads vertically, and thus the velocity in the central section ($y/B_0 = 0$) decreases (Figure 4f).

Profiles of transversal velocity show no clear transversal velocity in Case rf (Figure 5a), whereas there is strong evidence of transversal velocity toward the centerline in Case 1 (Figure 5c). In both cases, the transverse profile of

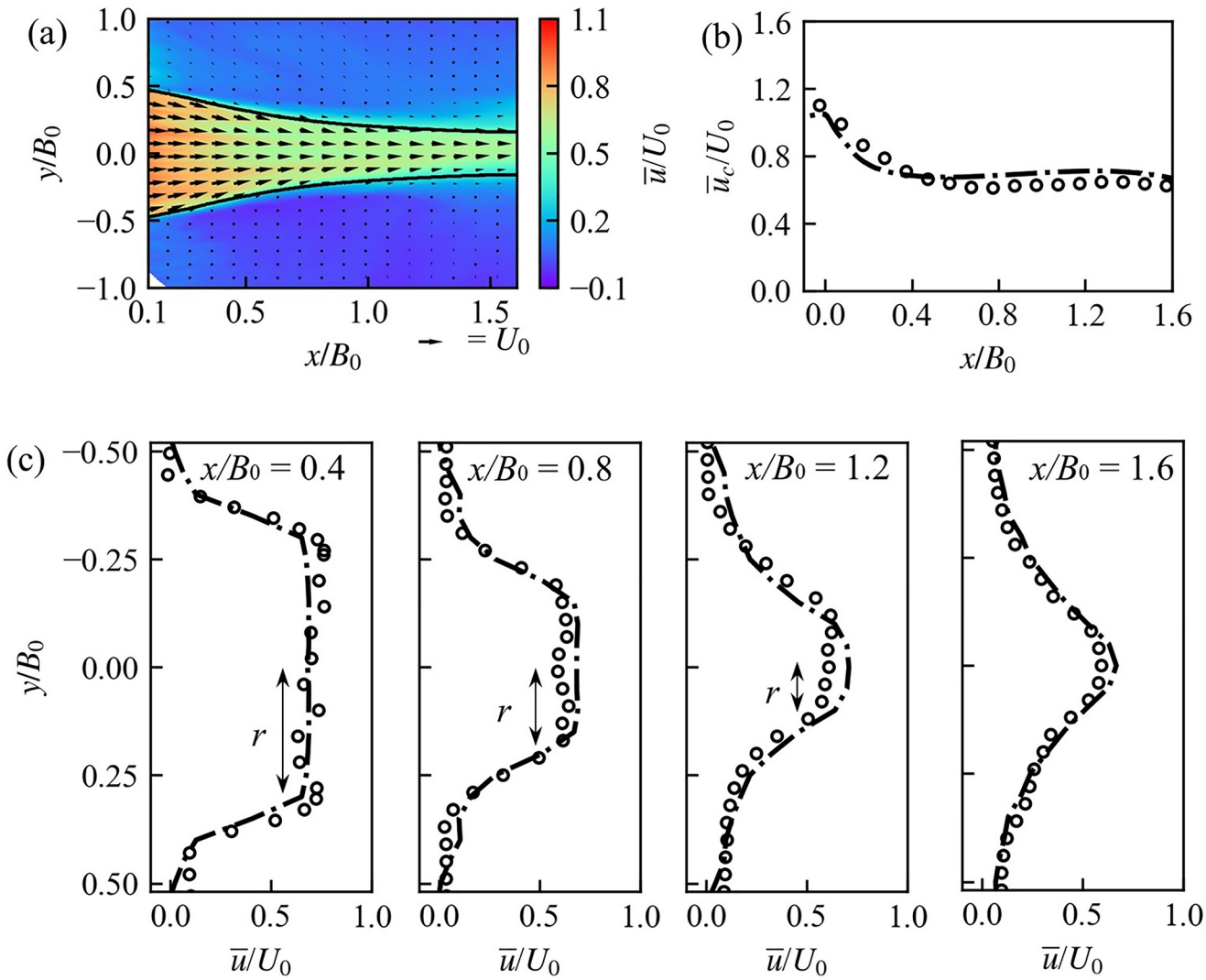

Figure 3. Velocity distributions in Case 1 at $z/H_0 = -0.5$. (a) Measured velocity distribution. The black solid line marks the boundary of the jet based on its width b calculated from the numerical model (see Figure 5e). Legend: range of velocity. (b) Measured (circles) and modeled (dashed-dotted line) longitudinal velocity profile along the centerline. (c) Measured (circles) and modeled (dashed-dotted lines) transverse profiles of the longitudinal velocity at $x/B_0 = 0.4$, 0.8, 1.2, and 1.6; r indicates the half-width of the "top-hat."

longitudinal velocity gradually transforms from a "top-hat" profile into a Gaussian distribution (Figures 5b and 5d), matching well with the Gaussian profile for a quasi-2D plane jet suggested by e.g., Deo et al. (2008):

$$\frac{U(y)}{U_c} = \exp\left(-\frac{4y^2}{b^2}\ln 2\right) \quad (1)$$

The location where the Gaussian profile is formed defines the transition point (x_T) from the flow establishment zone to the established flow zone. This transition point is much closer to the channel mouth in Case 1 ($x_T/B_0 \approx 1.6$) than in Case rf ($x_T/B_0 \approx 4$). Cohen (2012) also obtained $x_T/B_0 \approx 4$ for the location of the transition point for the plane jet over a horizontal bottom from experiments. Based on the transverse profile of longitudinal velocity (Figures 5b and 5d), jet width b was calculated and is shown in Figure 5e; $b = 2|y_{0.5}|$ where $y_{0.5}$ denotes the transverse coordinate and where the longitudinal velocity is 50% of the centerline velocity U_c. The thickness of jet h_c in the central section ($y/B_0 = 0$) is calculated following Lee and Yu (1997): $h_c = \left(\int_{z_b}^{0} \overline{u}_c dz\right)^2 / \int_{z_b}^{0} (\overline{u}_c)^2 dz$, with u_c being centerline velocity and z_b, bottom depth. In Case rf, jet thickness is constant ($\approx H_0$) while its width increases

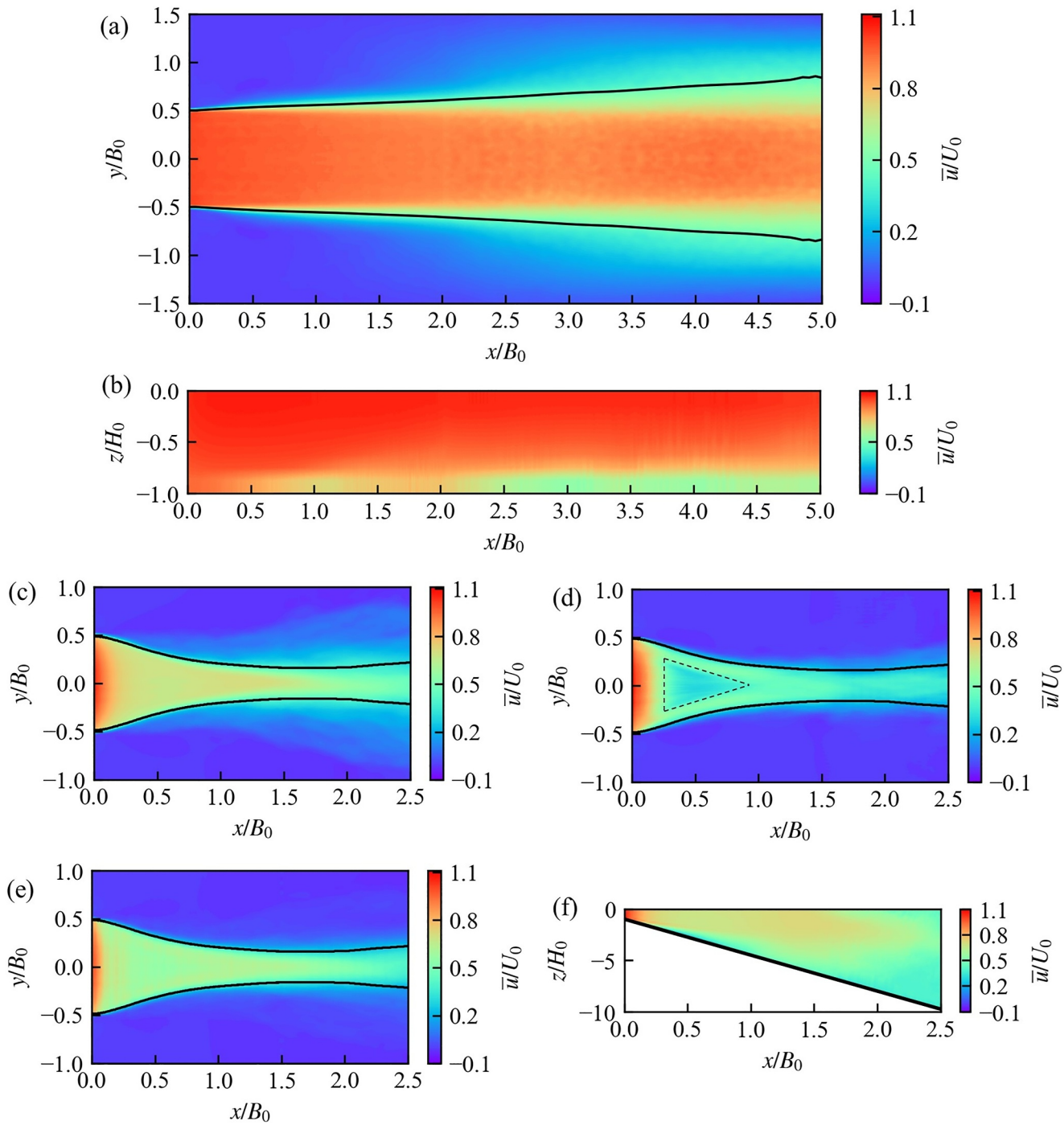

Figure 4. Time-averaged velocity distribution for Case rf: (a) in a horizontal plane at $z/H_0 = -0.5$ (solid lines show jet width) and (b) at the central-section ($y/B_0 = 0$). (c–e) Time-averaged velocity distribution for numerical Case 1: (c) in a horizontal plane at $z/H_0 = -0.5$, (d) in an inclined plane 2 cm above the sloping bottom boundary (dashed-lined triangle denotes a region with relatively lower velocity inside the jet), and (e) depth-averaged velocity field. (f) Velocity distribution at the central section ($y/B_0 = 0$) for numerical Case 1.

due to entrainment of ambient fluid (e.g., Pope, 2000; Figure 5e, dashed lines). In the presence of a sloping bottom, fluid momentum is also spread in the vertical direction (h_c increases) and thus width b decreases (Figure 5e, solid lines). The jet's vertical thickness (h_c) in this case is close to the local water depth ($H = x \tan\beta + H_0$, Figure 5e, gray dash-dotted line). As the jet thickness increases, the shear surface between the jet and ambient water increases, resulting in more entrainment of ambient water into the jet. The two competing effects

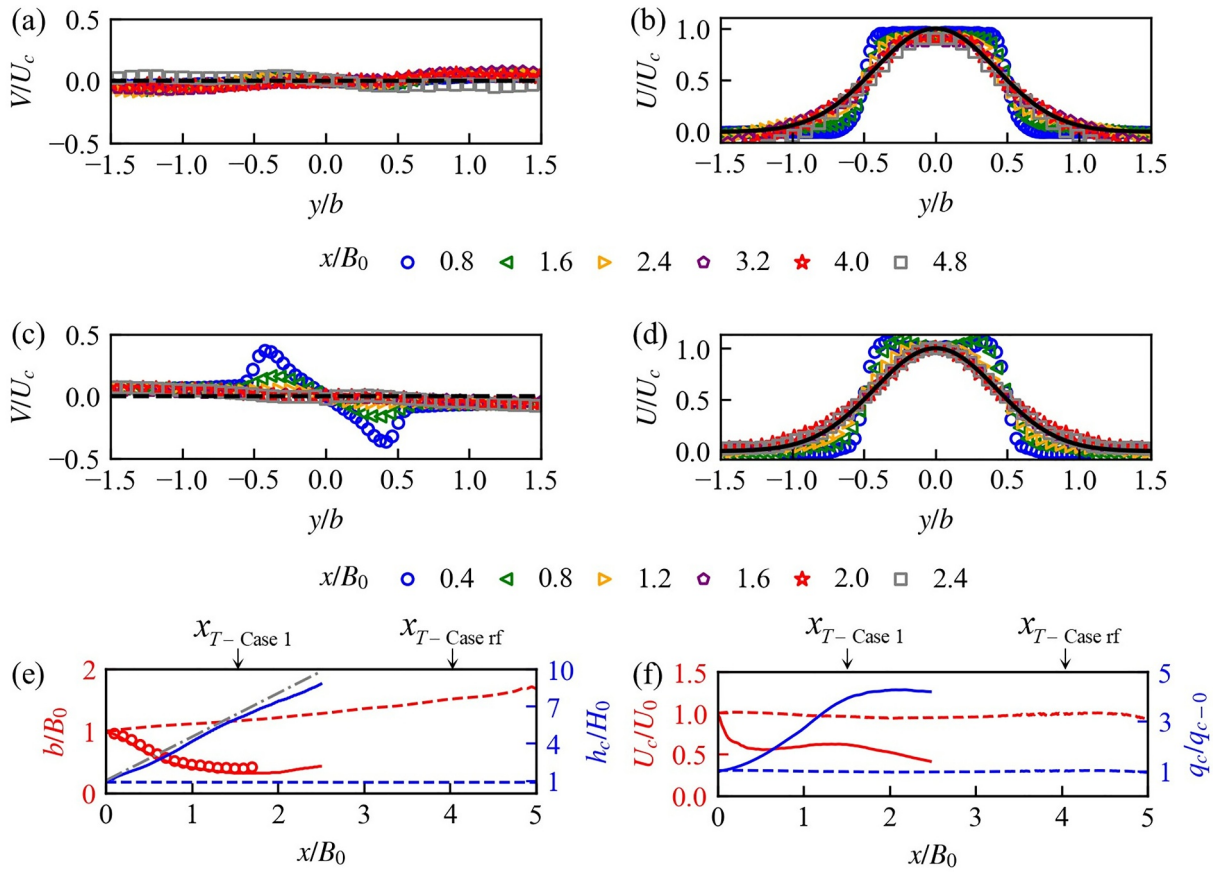

Figure 5. Transverse distribution of depth-averaged transversal and longitudinal velocity for numerical Case rf (a and b) and Case 1 (c and d). Black dashed line in (a) and (c) is zero. Black solid line in (b) and (d): Gaussian profile (Equation 1). Legends for (a–d): symbols related to the longitudinal coordinates. (e) Variations of the jet width (red) and jet thickness (blue) in numerical Case 1 (solid lines) compared with reference Case rf (dashed lines). The red circles denote the jet width obtained from the measured velocity field at $z/H_0 = -0.5$. Gray dash-dotted line: increase of the local water depth for Case 1: $H = x\tan\beta + H_0$. (f) Variations of the depth-averaged centerline velocity (U_c/U_0; red) and discharge per unit width in the central section (blue; right vertical axis) for numerical Case rf (dashed lines) and Case 1 (solid lines).

(i.e., vertical extension and lateral entrainment) balance each other at a certain distance (here at $x/B_0 \approx 1.6$). Thereafter, entrainment becomes the dominant mechanism and width b slightly increases (Figure 5e, red solid line) as in Case rf. A comparison between Case rf and Case 1 in terms of depth-averaged centerline velocity and discharge per unit width in the central section ($q_c = U_c H$) shows that in Case rf, U_c, and q_c remain almost constant (Figure 5f). In contrast, in Case 1, a sharp decrease in U_c is observed in the range $0 < x/B_0 < 0.5$ (Figure 5f, red solid line) due to the increase of jet thickness (Figure 5e, blue solid line). After that, it undergoes a slight increase in the range $0.5 < x/B_0 < 1.6$, because q_c increases. The increase of q_c is triggered by transversal velocities directed toward the centerline (Figure 5c). For $x/B_0 > 1.6$, the transversal velocity becomes negligible, and thus, q_c remains almost constant and U_c decreases again.

Analytical models for the variation of jet width and centerline velocity for the sloping bottom case were proposed by Özsoy and Ünlüata (1982) and Ortega-Sánchez et al. (2008). Unlike the present study where $y_{0.5}$ is used to measure the jet width, they defined a jet half-width $\tilde{b}$ as the distance from the centerline to the location where the longitudinal velocity is equal to zero. They proposed the following relationship for the transverse profile of the longitudinal velocity in the flow establishment zone:

$$\frac{U(y)}{U_c} = F(\eta) = \begin{cases} 0 & \eta \geq 1 \\ \left(1-\eta^{1.5}\right)^2 & 0 < \eta < 1 \\ 1 & \eta \leq 0 \end{cases} \quad \eta = \frac{|y|/\tilde{b} - r/\tilde{b}}{1 - r/\tilde{b}} \tag{2}$$

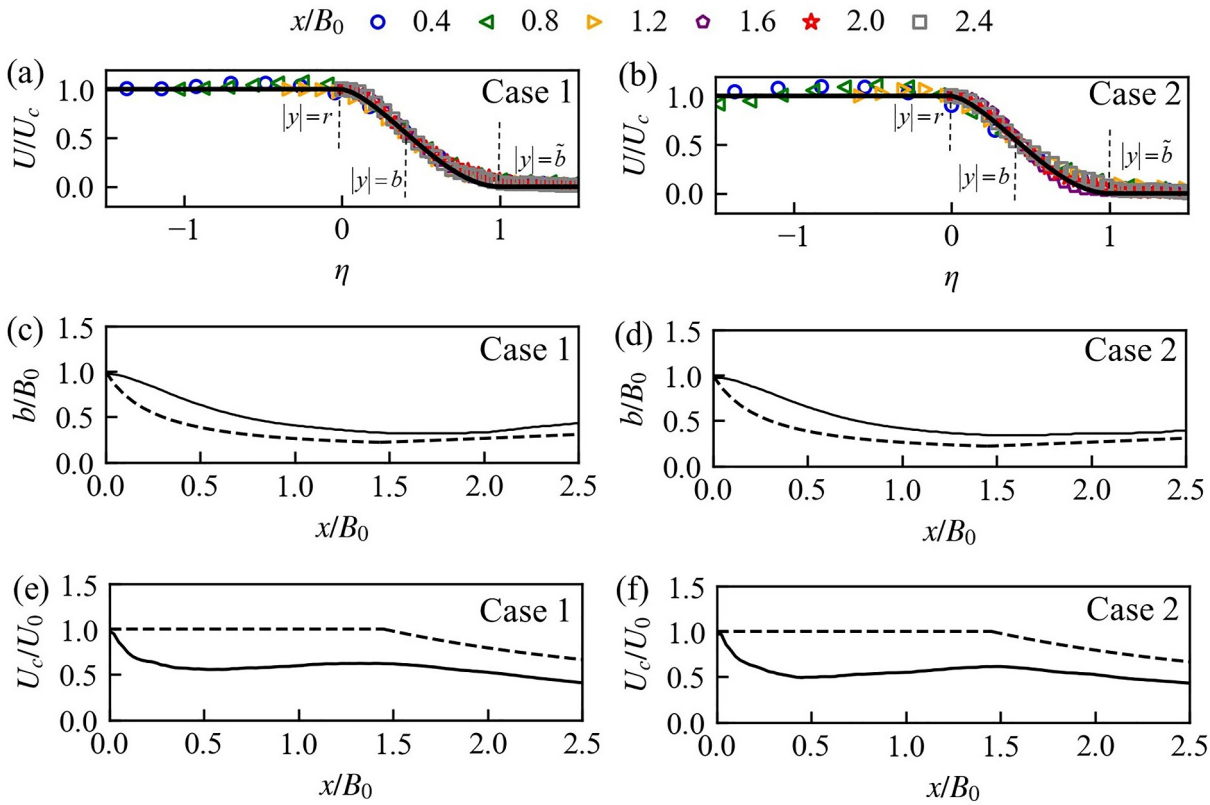

Figure 6. Transverse profiles of the longitudinal velocity for: (a) Case 1 and (b) Case 2 at different locations (x/B_0) indicated by colored symbols above the panels. Symbols: numerical data. Solid lines: results of Equation 2. Three typical locations $|y| = r$, b, and $\tilde{b}$ are identified by vertical dashed lines. Variation of jet width for: (c) Case 1 and (d) Case 2. Variation of centerline velocity for: (e) Case 1 and (f) Case 2. Solid lines: data from the numerical model. Dashed lines: predictions of the analytical model (Özsoy & Ünlüata, 1982).

with η being a similarity variable (Ortega-Sánchez et al., 2008). According to the definition, $U/U_c = 0.5$ when $y = \pm 0.5b$. Inserting this definition into Equation 2 gives $b = 0.88\tilde{b} + 1.12r$. This relationship and Equation 2 are compared with the present numerical data (Figures 6a and 6b). The abovementioned analytical models are based on time- and depth-averaged mass and momentum equations and include the bottom friction term expressed with the Darcy-Weisbach friction factor, which is set to $f = 0.02$ here. This corresponds to a Manning coefficient $n = H_0^{1/6}(8\ g/f)^{-0.5} \approx 0.01$, a typical value for smooth polyvinylchloride (PVC) surfaces. According to Ortega-Sánchez et al. (2008), the analytical model is not sensitive to f for slopes >3°. In the flow establishment zone, where $r > 0$, the models of Özsoy and Ünlüata (1982) and Ortega-Sánchez et al. (2008) are identical, derived from Equation 2, and assume that the centerline velocity remains constant. For the established flow zone, Equation 2 is still used in the model of Özsoy and Ünlüata (1982) by setting $r = 0$, while Ortega-Sánchez et al. (2008) used a hyperbolic secant function. Our numerical results are compared with the analytical model results of Özsoy and Ünlüata (1982) in Figures 6c–6f. The analytical results underestimate jet width and overestimate centerline velocity. Differences are due to the model assumption that there is a constant centerline velocity in the flow establishment zone ($x/B_0 < 1.6$). However, our numerical results (Figures 6e and 6f) and measurements (Figure 3b) demonstrate that the centerline velocity is not constant. In the established flow zone ($x/B_0 > 1.6$), the model roughly captures the variation of the jet width and centerline velocity if the curves are shifted upwards to compensate for the initial errors.

3.2. Turbulence Characteristics

Figures 7a and 7b presents the distribution of horizontal Turbulent Kinetic Energy (TKE), $k_H = 0.5\left(\overline{u'u'} + \overline{v'v'}\right)$, at $z/H_0 = -0.5$ for Case rf and Case 1. The vertical component of TKE is not available from the experimental data, but numerical model results confirm that the TKE is dominated by the horizontal components (Text S4 in

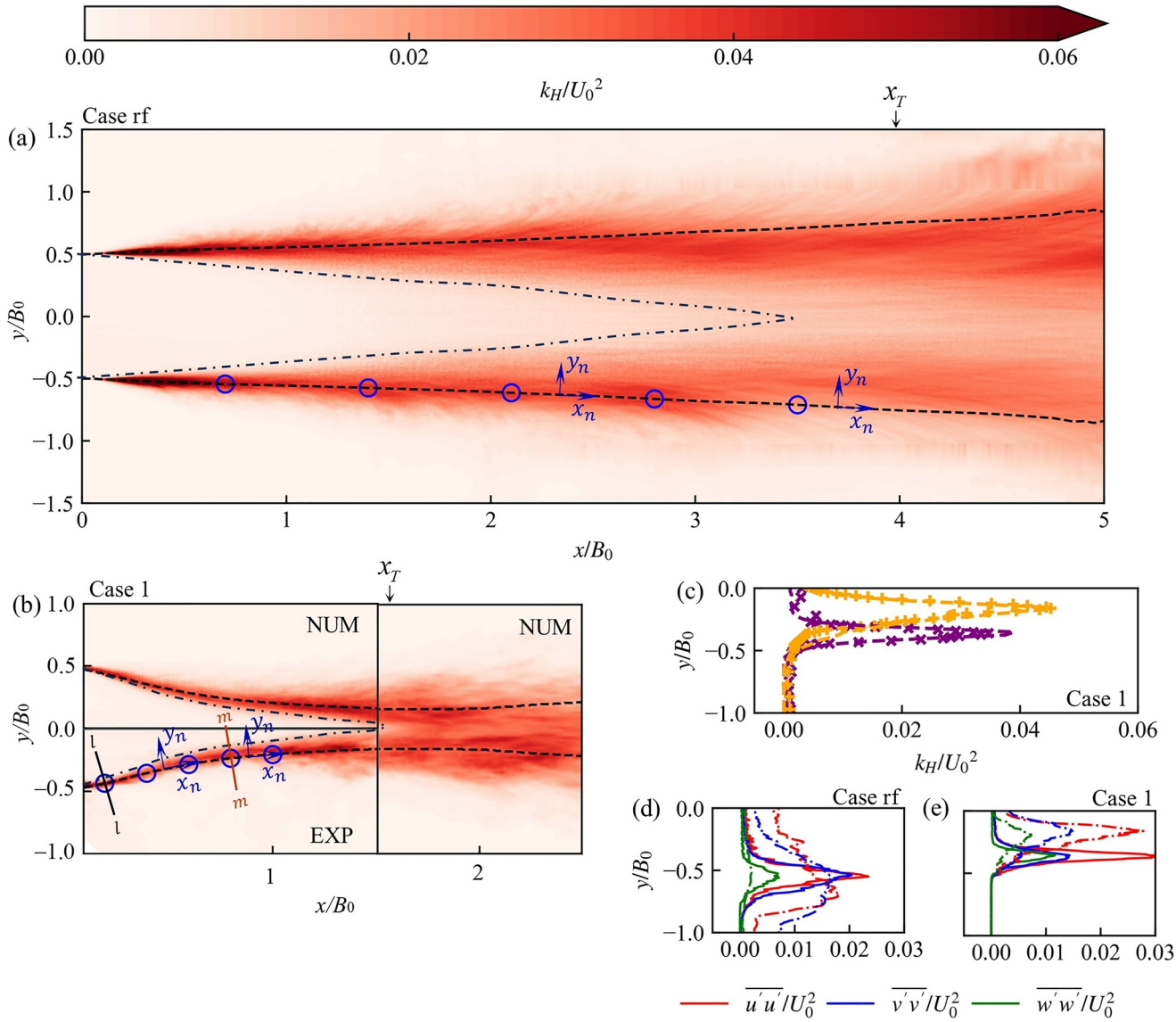

Figure 7. Distribution of horizontal turbulent kinetic energy k_H at $z/H_0 = -0.5$ for: (a) Case rf and (b) Case 1. For Case 1, in the region $x/B_0 < 1.5$, the upper half of the panel presents the numerical results (NUM), and the lower one, the experimental (EXP) data. In the region $x/B_0 > 1.5$, only numerical data are available. Dashed lines: jet width b. Dash-dotted lines: inner boundary of the shear layers, representing $k_H/U_0^2 = 0.01$. Five points (P1-5) on the jet width curve are shown by the blue circles in (a) and (b). For Case rf, these points are located at $x/B_0 = 0.7$, 1.4, 2.1, 2.8, and 3.5; for Cases 1 and 2, they are located at $x/B_0 = 0.2$, 0.4, 0.6, 0.8, and 1.0. A coordinate system corresponding to the jet width curve is represented by the blue arrows (x_n, y_n). In Case 1, lines l-l and m-m are two lines perpendicular to the jet width curve with intersections located at $x/B_0 = 0.2$ and 0.8, respectively. (c) Lateral distributions of k_H at $z/H_0 = -0.5$ at $x/B_0 = 0.4$ (purple), 1.2 (orange) in Case 1. Symbols: experimental data. Dashed lines: numerical data. Numerical transverse profiles of $\overline{u'u'}$ (red), $\overline{v'v'}$ (blue) and $\overline{w'w'}$ (green) for: (d) Case rf at $x/B_0 = 1$ (solid lines) and $x/B_0 = 3$ (dashed lines), and (e) Case 1 at $x/B_0 = 0.4$ (solid lines) and $x/B_0 = 1.2$ (dashed lines). In plots (c–e), only half of the jet is presented.

Supporting Information S1). Shear layers with large k_H values are observed along each side of the jet. Although the two shear layers in Case rf remain almost parallel to each other, since they grow laterally with increasing offshore distance, the inner boundaries of the two shear layers (dash-dotted line, representing $k_H/U_0^2 = 0.01$) move toward the centerline and meet at $x/B_0 = 3.6$, which is close to the transition point from the flow establishment zone to the established flow zone ($x_T/B_0 \approx 4$). In contrast, the jet undergoes a lateral convergence in sloping bottom Case 1. As a result, the shear layers meet at $x/B_0 = 1.55$, which is much closer to the channel mouth, and is again very close to the transition point from the flow establishment zone to the established flow zone ($x_T/B_0 \approx 1.6$). Similar to Case rf, the width of the region with high k_H values widens with increasing offshore distance, indicating that the lateral shear layers are spreading. The close resemblance between experimental and

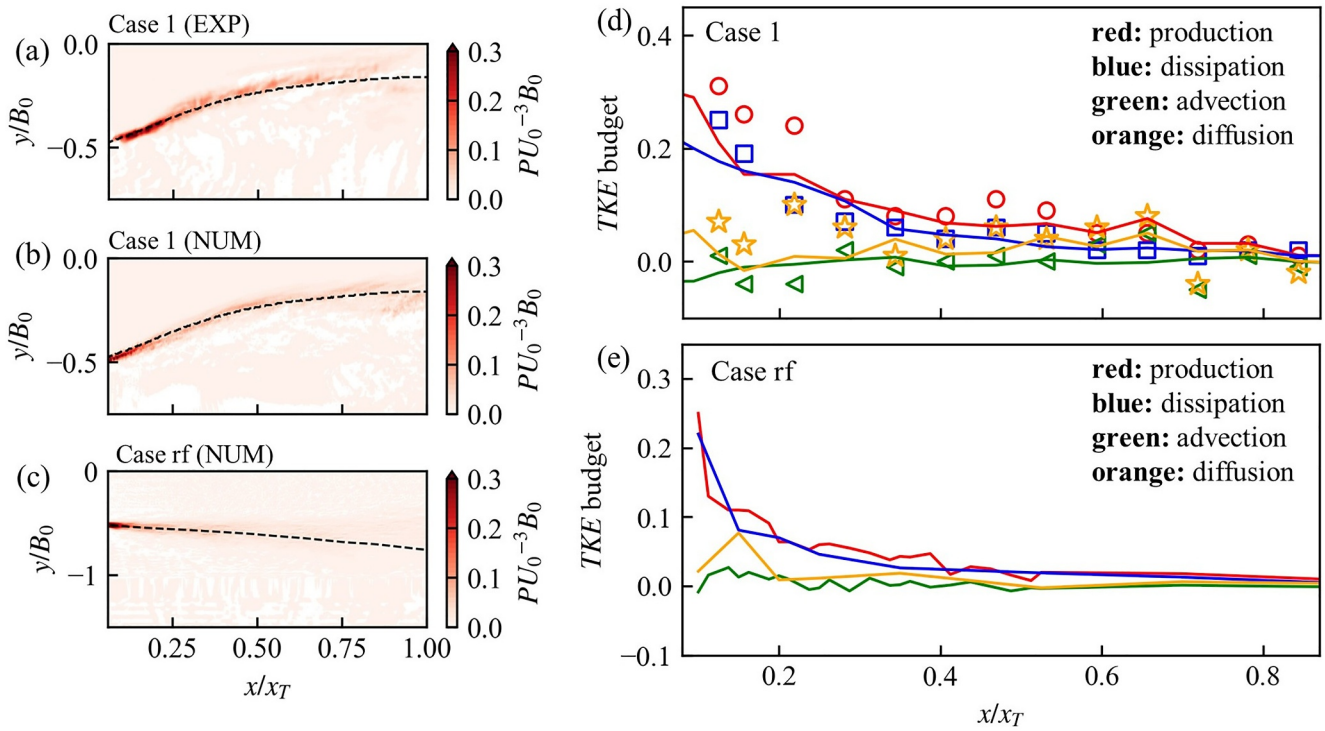

Figure 8. TKE production rate (P, Equation 3) at $z/H_0 = -0.5$ for: (a) Case 1 experimental (EXP) data, (b) Case 1 numerical (NUM) data, and (c) Case rf numerical data. Considering that the system is symmetric, only half of the domain ($y < 0$) is plotted. (d and e) TKE budget analysis along the jet-ambient interface (dashed lines in panels a–c) for Case 1 (d) and Case rf (e). Symbols represent experimental data while lines represent numerical results. Terms are nondimensionalized using U_0 and B_0.

numerical transverse profiles of k_H (Figure 7c), confirms that our numerical model can reproduce the main turbulence features. The magnitudes of $\overline{u'u'}$, $\overline{v'v'}$, and $\overline{w'w'}$ are compared in Figures 7d and 7e based on the numerical data. In Case rf, $\overline{u'u'}$ and $\overline{v'v'}$ are similar in magnitude and larger than $\overline{w'w'}$. In Case 1, however, both $\overline{v'v'}$ and $\overline{w'w'}$ are much smaller than $\overline{u'u'}$. More detailed comparisons of the horizontal and vertical components of TKE are presented in Text S4 of the Supporting Information S1.

Below, the focus is on the turbulence characteristics of the shear layers in the flow establishment zone before they merge with each other. The turbulent kinetic energy budget is (Panchapakesan & Lumley, 1993; Pope, 2000):

$$P + \left(-\frac{1}{2}u_i\frac{\partial \overline{u_i u_i}}{\partial x_i}\right) - \varepsilon - D = 0 \tag{3}$$

Terms in Equation 3 are, respectively, production, advection, dissipation and diffusion. The TKE production rate ($P = -\overline{u_i'u_j'}\partial\overline{u}_i/\partial x_j$) is generally positive and thus a source of TKE. It describes the energy transfer from the mean velocity gradients (working against the Reynolds stresses) to fluctuating velocity fields. P was determined based on the measured and modeled horizontal velocity fields, since vertical velocities were not measured and the horizontal components are the main source (Text S4 in Supporting Information S1). In Case rf and Case 1, P is strong inside the shear layer, in particular close to the channel mouth (Figures 8a–8c). Further away from the channel mouth as the shear layer develops, P decreases because of the decrease of the velocity gradient (Figures 4a and 4c). The TKE budget was analyzed along the jet-ambient interface (determined by the jet width; dashed lines in Figures 7a, 7b, and 8a–8c) and shown in Figures 8d and 8e. The advection term was calculated as defined in Equation 3, but neglecting the vertical components. The TKE dissipation rate ε was estimated using the inertial-dissipation technique based on the energy spectrum (Geyer et al., 2010; Shaw & Trowbridge, 2001; Siebert et al., 2006). The diffusion term is difficult to determine accurately (e.g., Pope, 2000). Therefore, it was calculated using Equation 3 after all other terms were calculated. Figures 8d and 8e shows that the TKE production is mainly dissipated locally while the rest is balanced by diffusion. The advection term is comparatively small and its value may be due to the uncertainty when calculating TKE gradients.

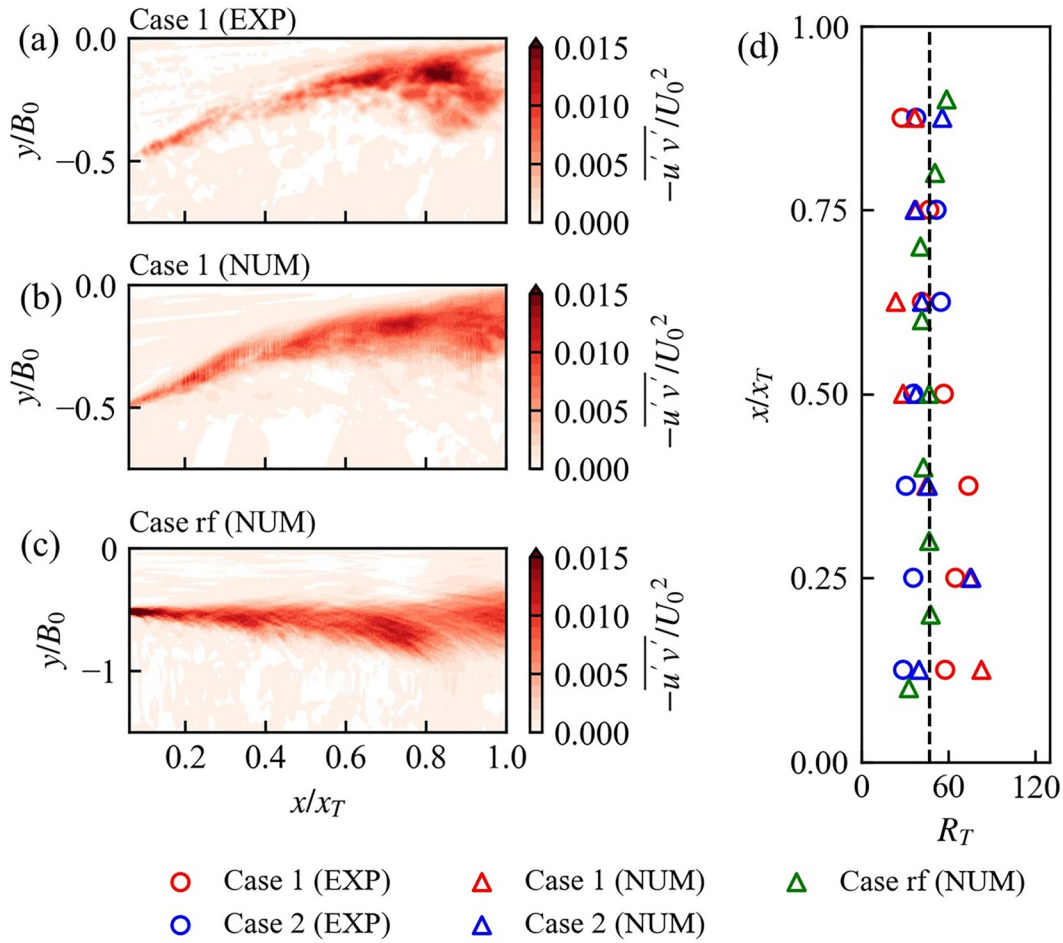

Figure 9. Distribution of $-\overline{u'v'}$ at $z/H_0 = -0.5$ for: (a) Case 1 experimental data, (b) Case 1 numerical data, and (c) Case rf numerical data. Considering that the system is symmetric, only half of the domain ($y < 0$) is plotted. (d) Turbulent Reynolds number averaged over the shear layers at $z/H_0 = -0.5$. Black vertical dashed line in (d): average value of R_T over all data sets in this panel (see legend).

Like TKE (Figures 7a and 7b), the horizontal Reynolds stress ($-\overline{u'v'}$) at $z/H_0 = -0.5$ is high in the shear layer (Figures 9a–9c). In the region $0.75 < x/x_T < 1.0$ in Case 1 where the two shear layers are close to each other, the magnitude of the Reynolds stress is larger than near the channel mouth. This phenomenon is not observed in Case rf. Turbulent viscosity $\upsilon_t = -\overline{u'v'}/(\partial\overline{u}/\partial y)$ is an important parameter that is often used for shear stress closure (e.g., Odier et al., 2012; Shih et al., 1995; Shiono & Knight, 1991). It can be nondimensionalized into a turbulent Reynolds number $R_T = (0.5b - r)\,\overline{u}_c/\upsilon_t$. Considering that measured/modeled values of turbulent viscosity are not reliable close to the lateral boundary of a shear layer (Odier et al., 2012), R_T is averaged inside the shear layers between $y_{0.8}$ and $y_{0.2}$ (Figure 9d); $y_{0.8}$ and $y_{0.2}$ represent the locations of 80% and 20% of the centerline velocity $\overline{u}_c$, respectively. No clear difference between Case rf and Cases 1 and 2 is observed in terms of R_T (Figure 9d). Combining all experimental and numerical data in Figure 9d, an averaged value of $R_T \approx 47 \pm 14$ was obtained, which is larger than the theoretical value ($R_T \approx 31$) for a self-similar 2D plane jet (Pope, 2000). This may indicate that classical 2D theory overestimates the Reynolds stress in a jet flowing over a solid bottom as was already reported by Rowland et al. (2009) for a horizontal bottom jet.

3.3. Characterization of the Shear Layers

A new coordinate system (x_n, y_n) is defined as one that follows the jet width curve (dashed lines in Figures 7a and 7b) with corresponding velocities $u_n = \overline{u}_n + u'_n$ tangent to the curve, and $v_n = \overline{v}_n + v'_n$ perpendicular to the curve. Directions of (x_n, y_n) do not show substantial differences with the original coordinates (x, y) in Case rf. However,

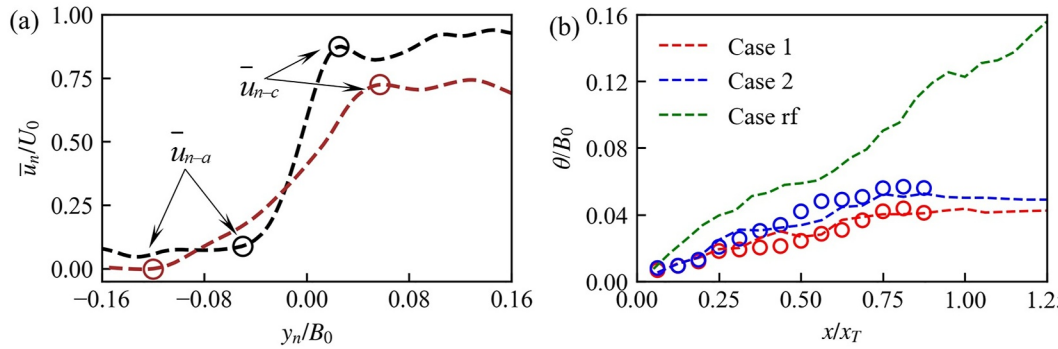

Figure 10. (a) Typical velocity profiles along lines *l-l* (black) and *m-m* (brown) shown in Figure 7b for Case 1. Ambient waters ($\overline{u}_{n-a}$) and jet ($\overline{u}_{n-c}$) values are marked by circles. (b) Variations of the shear-layer momentum thickness. Circles: experimental data. Lines: numerical data. Red: Case 1. Blue: Case 2. Green: Case rf.

in Case 1, (x_n, y_n) is a curvilinear coordinate system with changing directions because the jet converges. Following the y_n direction, velocity $\overline{u}_n$ must increase from a small value $\overline{u}_{n-a}$ (at y_{n-a}) in the ambient water to a large value $\overline{u}_{n-c}$ inside the jet (at y_{n-c}). Typical profiles of measured $\overline{u}_n$ in Case 1 are plotted in Figure 10a.

Momentum thickness θ is a characteristic length scale that describes the width of a shear layer (Ho & Huang, 1982; Rogers & Moser, 1992):

$$\theta = \int_{y_{n-a}}^{y_{n-c}} \left[\frac{1}{4} - \left(\frac{\overline{u}_n - \overline{u}_{n-o}}{\overline{u}_{n-c} - \overline{u}_{n-a}} \right)^2 \right] dy_n \tag{4}$$

where $\overline{u}_{n-o}$ is the arithmetic mean of $\overline{u}_{n-a}$ and $\overline{u}_{n-c}$. The variation of θ along x was calculated using the experimental and numerical velocity fields (Figure 10b). The momentum thickness continuously increases with x in Case rf. In the sloping bottom Cases 1 and 2, it first increases and then becomes almost constant after $x/x_T > 1$. The momentum thickness is comparatively smaller in Case 1 with larger Fr_0 and Re_0 than Case 2 (Table 1), which is consistent with previous findings in slowly spreading shear layers (Dimotakis, 1991).

3.4. Turbulent Coherent Structures

3.4.1. Structure Identification and Strouhal Numbers

Kelvin Helmholtz-type Coherent Structures (KHCS) are often observed in shear layers (Brown & Roshko, 1974). KHCS were also seen in the discharge from an outlet in the coastal environment (Figure 2) and are therefore an important feature of the exchange flow between a water body passing through a channel and the receiving ocean or lake. The transient iso-concentration surface ($c = 0.7$) in numerical Case 1 indicates the occurrence of KHCS (Figure 11). Concentration c is determined by the degree of mixing of two fluids, that is, $c = 1$ inside the inflow channel, and $c = 0$ in the ambient water (see Text S2 in Supporting Information S1). Thus, the iso-concentration surface ($c = 0.7$) in Figure 11 is composed of 70% inflow water and 30% ambient water. The turbulent structures generate nearly periodic local velocity fluctuations in the velocity time series (Figures 12a and 12b). The Power Spectral Density (PSD) is obtained from the velocity signals at locations P1-P5 (blue circles in Figures 7a and 7b) on the jet-ambient interface; the Strouhal number $St_\theta = f\theta/\overline{u}_{n-o}$ is used as the nondimensional frequency (Ho & Huerre, 1984). All spectra have a strong peak close to $St_\theta = 0.079$ indicating the dominant KHCS frequency. This Strouhal number (~0.079) is consistent with the typical value of KHCS in slowly spreading shear layers (Ho & Huang, 1982; Ho & Huerre, 1984).

3.4.2. Contribution of KHCS to Momentum Exchange and Energy Production

KHCS contribute to the momentum exchange and production of TKE in shear layers (Taborda et al., 2022; Truong & Uijttewaal, 2019; White & Nepf, 2008). The momentum exchange between the jet and ambient waters is mainly represented by the horizontal Reynolds stress $-\overline{u_n' v_n'}$ at the interface ($y_n = 0$) (Taborda et al., 2022;

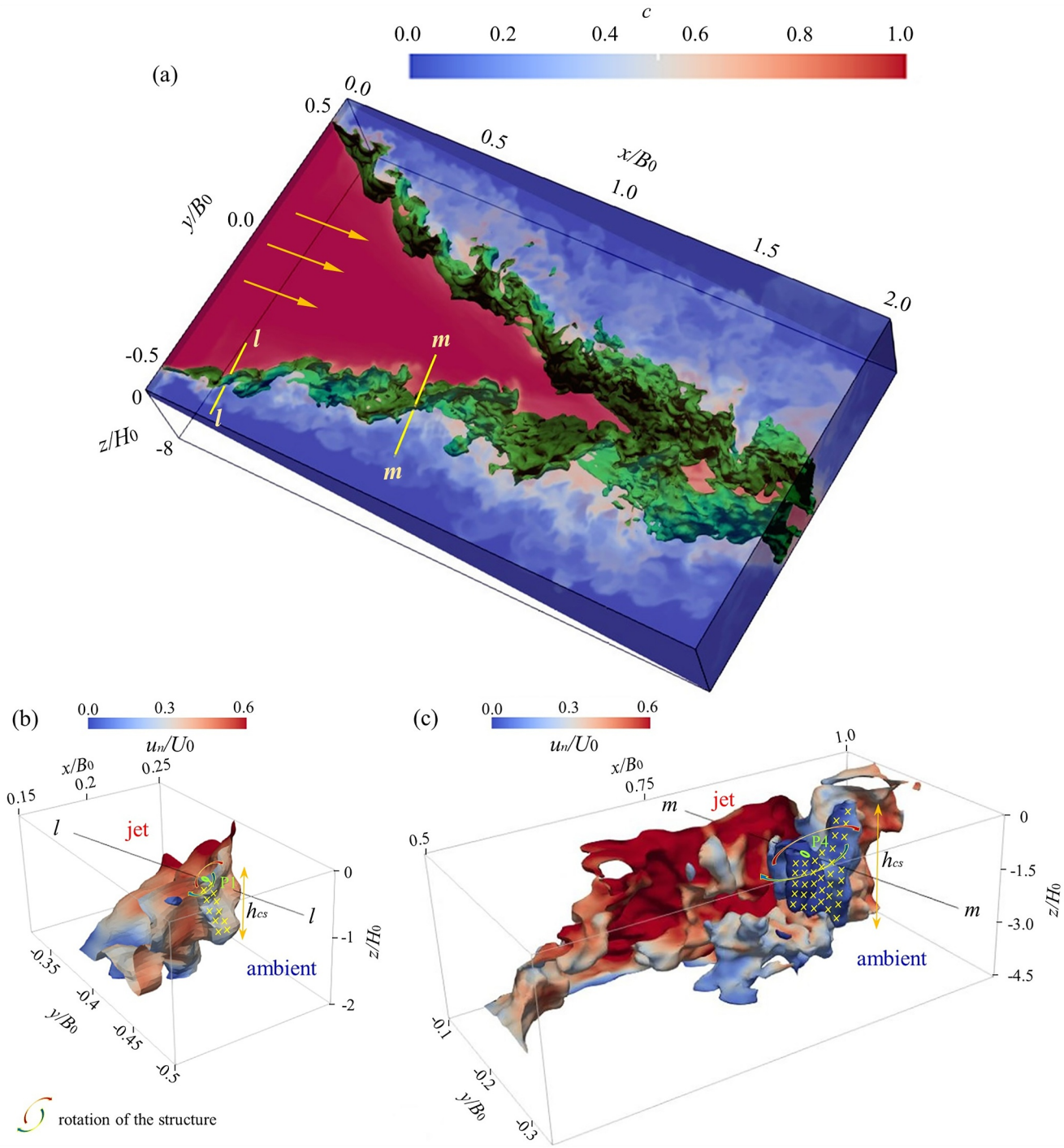

Figure 11. (a) Instantaneous field of concentration c for numerical Case 1. The translucent background color (from blue to red in legend) illustrates the concentration distribution in the 3D field. The iso-concentration surface for $c = 0.7$ is highlighted in green. Arrows: inflow direction. Details of the iso-concentration surface $c = 0.7$: (b) in the region of line l-l, and (c) in the region of line m-m; see colorbar for u_n. Regions with relatively small u_n values (sometimes even turning backwards) of Kelvin Helmholtz-type Coherent Structures (KHCS) are highlighted by yellow crosses. The KHCS thickness is given by h_{cs}. The sense of rotation and the size of the KHCS are indicated by the curved arrows.

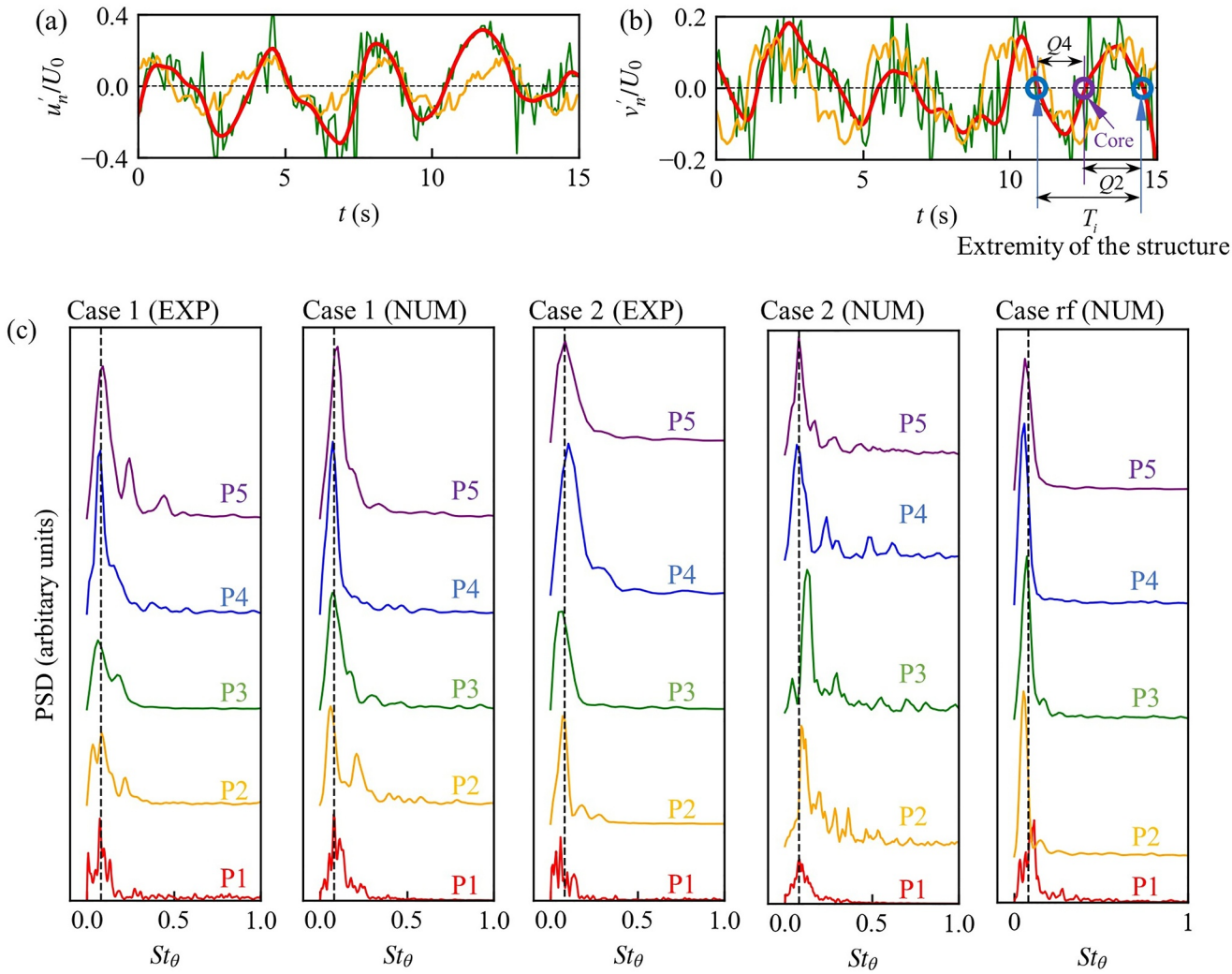

Figure 12. (a) and (b): Fluctuating velocities measured at P1 (for location of P1, see Figure 7b) for experimental Case 1. Green lines: raw data. Red lines: low-pass filtered data. Orange lines: conditionally averaged data. Horizontal dashed lines are zero. $Q2$: Quadrant 2 (ejection), $Q4$: Quadrant 4 (sweep). (c) Power spectral density of experimental (EXP) and numerical (NUM) velocity fluctuations at locations P1-5 as a function of the Strouhal number for Cases 1, 2 and rf (for locations of P1-5, see Figures 7a and 7b). The vertical dashed lines mark $St_\theta = 0.079$.

Truong & Uijttewaal, 2019). The TKE production rate P_n in the curvilinear coordinate system (neglecting vertical components) is given by,

$$P_n = -\left(\overline{u_n' u_n'}\frac{\partial \overline{u}_n}{\partial x_n} + \overline{v_n' v_n'}\frac{\partial \overline{v}_n}{\partial y_n} + \overline{u_n' v_n'}\frac{\partial \overline{u}_n}{\partial y_n} + \overline{u_n' v_n'}\frac{\partial \overline{v}_n}{\partial x_n}\right) \quad (5)$$

To compare the contribution of KHCS and small-scale turbulence to momentum exchange and TKE production, it is necessary to separate the velocity fluctuations associated with KHCS from those associated with small-scale turbulence. This analysis was only based on the experimental data of Case 1. Case rf could not be investigated because the LES model does not directly resolve small-scale turbulence.

Two different methods were proposed in the literature to quantify the contribution of KHCS: The first method uses a simple low-pass filter to separate low-frequency (associated with KHCS) from small-scale, turbulence-induced high-frequency velocity signals (Li et al., 2022; Truong & Uijttewaal, 2019). Examples of filtered velocity signals are shown in Figures 12a and 12b (using a low-pass filter, $f_{\text{filter}} = 4f_{cs}$ following Truong and Uijttewaal (2019)); f_{cs} is the dominant frequency of KHCS, that is, peak frequency in Figure 12c before nondimensionalization.

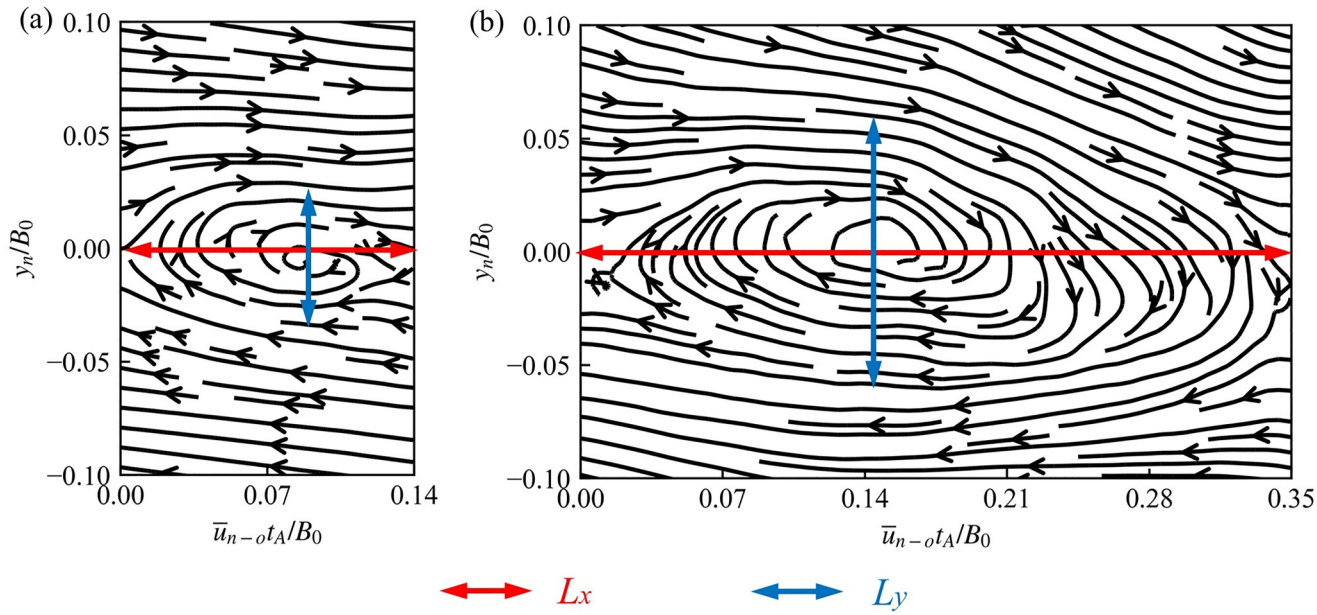

Figure 13. Streamlines of the conditionally averaged velocity field relative to a reference frame moving with the Kelvin Helmholtz-type Coherent Structures (KHCS). (a) Structure passing line *l-l*. (b) Structure passing line *m-m*. Results are based on experimental data from Case 1; for locations of lines *l-l* and *m-m*, see Figure 7b. L_x and L_y give the dimensions of the KHCS along (red) and across (blue) the interface between the jet and the ambient waters. Note that L_x and L_y are scaled differently.

In the second method, the measured flow field is reconstructed based on conditional-averaging in order to smooth out small-scale turbulence (Shi et al., 2023; Taborda et al., 2022; Yuan & Horner-Devine, 2017). The conditional-averaging approach identifies KHCS using three consecutive zero-crossings of low-pass filtered v_n' (Taborda et al., 2022; White & Nepf, 2008), based, for example, on the velocity signal at P1 (Figure 12b). A typical KHCS (Figure 12b) lasts for a time period of T_i and contains a sweep ($Q4$) and an ejection ($Q2$) event, as distinguished using quadrant analysis (Bagherimiyab & Lemmin, 2018; Huai et al., 2019; Nezu & Nakagawa, 1993; White & Nepf, 2008). Results of a quadrant analysis of velocity signals are given in Text S5 of the Supporting Information S1. A series of KHCS is identified based on low-pass filtered data, which provide the starting and ending time of a given structure (Taborda et al., 2022). The measured flow field (before low-pass filtering) of the identified structures along line *l-l* during their periods T_i is then rescaled into a new time coordinate $t_A = T_d(t - t_0)/T_i$, where $T_d = 1/f_{cs}$. Here, t is the instantaneous raw time and t_0 is the time when the structure first appears (Taborda et al., 2022). Rescaled velocity signals of the identified structures are then averaged to obtain the conditionally averaged data. Note that the conditionally averaged velocity field obtained here is based on the "raw" measured data rather than on the low-pass filtered data; the low-pass filtered data were only used to identify coherent structures. According to Taylor's frozen hypothesis, the structures are advected mainly by the mean velocity. The conditionally averaged velocity field relative to a reference frame moving with a velocity $\overline{u}_{n-o}$ is obtained by subtracting this reference velocity. The same procedure is also applied to the velocity signals of P4 to determine the structures on line *m-m*. The conditionally averaged flow field provides streamline patterns of the KHCS (Figure 13). Compared with the structure at line *l-l*, the structure at *m-m* is larger in both the x_n (L_x) and y_n (L_y) directions. Since coherent structures are induced by shear and located inside the shear layer, the size of the structure defined by L_x and L_y scales with the width of the shear layer, that is, $L_x \sim L_y \sim \theta$. Thus, the time period of the structure is $T_d = 1/f_{cs} = L_x/\overline{u}_{n-o} \sim \theta/\overline{u}_{n-o}$, which explains why the Strouhal number remains almost constant (Figure 12c).

Low-pass filtered or conditionally averaged flow fields were used to calculate Reynolds stress and second-order terms in P_n (i.e., $\overline{u_n'u_n'}$, $\overline{u_n'v_n'}$, $\overline{v_n'v_n'}$) associated with KHCS (Figure 14). Based on the low-pass filtering method, low-frequency signals contribute 78% and 79% of the total momentum exchange at P1 and P4, respectively. These values change, respectively, to 63% and 68% if the conditionally averaged method is applied. For the TKE production rate, the integral of P_n from $y_n/B_0 = -0.15$ to 0.15 was calculated. Based on the low-pass filtering method, the low-frequency signals contributed 72% and 79% to the total production rate at lines *l-l* and *m-m*,

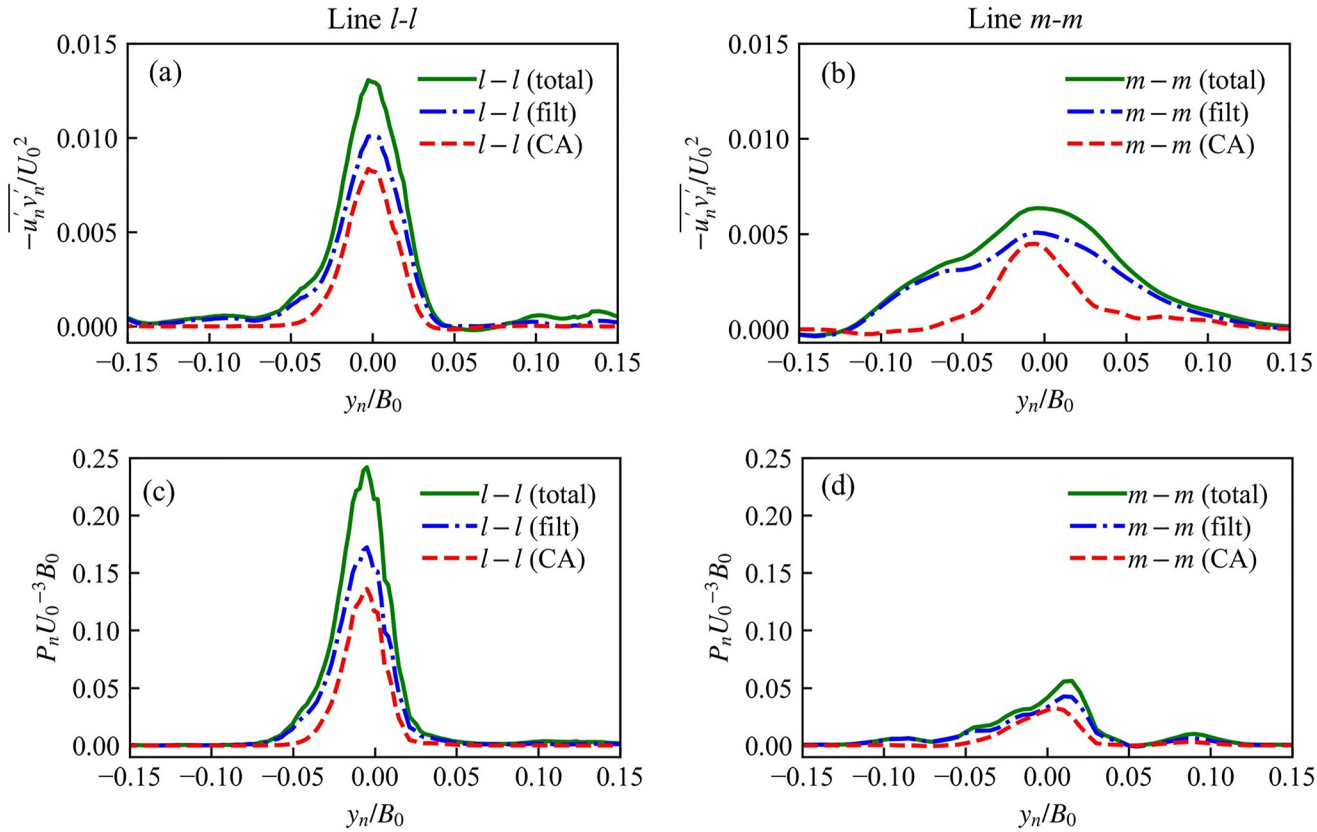

Figure 14. Horizontal Reynolds stress (top panels) and TKE production rate (bottom panels) induced by the Kelvin Helmholtz-type coherent structures compared to total horizontal Reynolds stress and TKE production rate for experimental Case 1. Left panels: along line *l-l*. Right panels: along line *m-m* (for location, see Figure 7b). Green solid lines: total values. Blue dashed-dotted lines: low-pass filtered values (filt). Red dashed lines: conditionally averaged values (CA).

respectively. If the conditional-averaging method is applied, these values are 45% and 50%, respectively. The processed velocity data obtained by the two different methods mentioned above are compared in Figures 12a and 12b. Using the low-pass filter, the velocity signals are smoothed, but the variations of the KHCS are preserved, that is, the three KHCS identified in Figure 12b have slight differences in terms of time period and fluctuation amplitude. Such variability of KHCS is smoothed out when the conditional-averaging method is used. This explains why KHCS-associated momentum exchange and TKE production rate are underestimated using conditionally averaged data.

3.4.3. Vertical Extent of KHCS

The vertical thickness of the plane jet for the horizontal-bottom case remains constant (equal to H_0; Figure 5e, blue dashed line). The jet over an 8° sloping bottom, on the other hand, spreads vertically with increasing water depth (Figure 5e, blue solid line), and as a result, the vertical thickness (h_{cs}) of KHCS increases with the increase of jet thickness (Figure 11). KHCS are characterized by regions with relatively small u_n (sometimes even turning backwards; see yellow crosses in Figures 11b and 11c). Autocorrelations of the modeled concentration c at P1 and P4 (at $z_c/H_0 = -0.5$), along with cross-correlations R_{zz} with points at different depths were determined using (Bagherimiyab & Lemmin, 2018; Nezu & Nakagawa, 1993):

$$R_{zz}(x,y,z_c : z,\sigma) = \frac{\overline{c'(x,y,z_c,t)c'(x,y,z,t+\sigma)}}{\sqrt{\overline{\left[c'(x,y,z_c,t)\right]^2}\overline{\left[c'(x,y,z,t+\sigma)\right]^2}}} \quad (6)$$

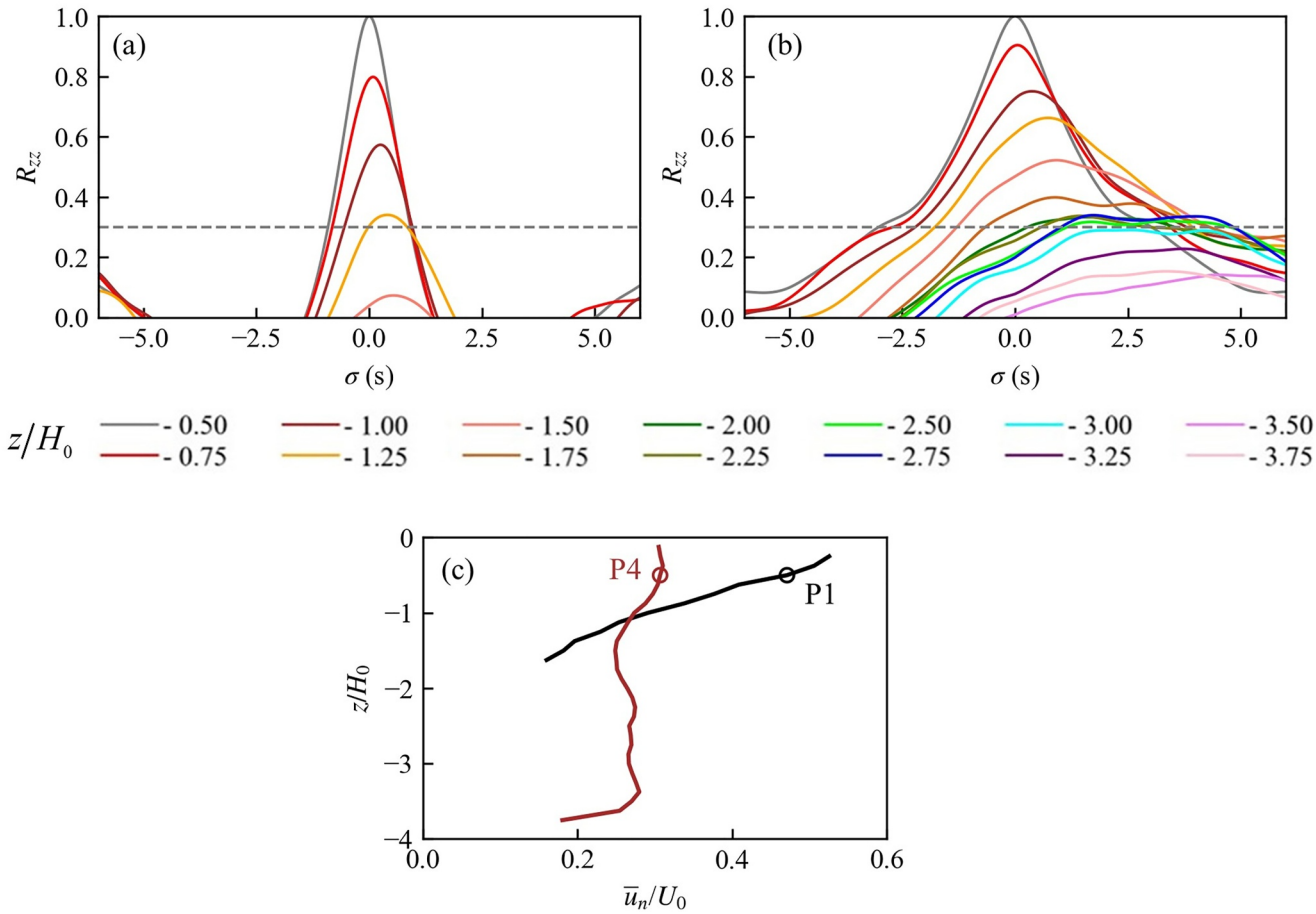

Figure 15. Autocorrelation for concentration signals at $z_c/H_0 = -0.5$ and cross-correlation values between $z_c/H_0 = -0.5$ and elevations below $z_c/H_0 = -0.5$, at: (a) P1 and (b) P4; colors defined in legend. The correlation values are calculated based on numerical data over 200 s (100 Hz) for Case 1. Horizontal dashed lines: threshold $R_{zz} = 0.3$. (c) Vertical profiles of the velocity $\overline{u}_n$ passing through points P1 (black line) and P4 (brown line); the points are marked by circles on the profiles (for location, see Figure 7b).

where σ is the time lag, and c' is concentration fluctuation. The cross-correlation decreases with increasing distance between the locations (Figures 15a and 15b), indicating that coherence is gradually lost. However, the loss of coherence at P4 (Figure 15b) is more gradual than at P1 (Figure 15a), confirming that the vertical thickness of the coherent structures increases with increasing distance from the channel mouth. Using $R_{zz} = 0.3$ as a threshold, the KHCS thickness increases from $1.25H_0$ (73% of local depth) at P1 to $2.75H_0$ (72% of local depth) at P4. The correlation time scale at P4 is longer than at P1. Moreover, a progressively larger positive time shift is observed when z increases. A positive time shift indicates that the concentration signal at a higher elevation correlates with the signal at a lower elevation at a later time. This suggests that the coherent structures are inclined, since $\overline{u}_n$ is comparatively larger close to the water surface (Figure 15c).

3.5. Merging of Lateral Shear Layers

When the plane jet reaches the established flow zone, the two shear layers meet and merge at the centerline (Figures 7a and 7b). After the shear layers merge, the jet may manifest a "flag-like" flapping motion (Antonia et al., 1983; Cohen, 2012; Oler & Goldschmidt, 1982; Rowland et al., 2009). Comparing the times series of depth-averaged concentration (c_d) at $x/x_T = 0.5$ and $x/x_T = 1$ for Case 1 and Case rf (Figure 16), it can be seen for both cases that at $x/x_T = 0.5$, the central part of the jet is stable and the KHCS only generate fluctuations at the sides of the jet. At $x/x_T = 1$, however, the jet flaps, showing a meandering pattern. The frequency of the jet flapping motion (f_j) was obtained from spectral analysis of the velocity at the centerline (i.e., the peak of PSD of the depth-averaged transversal velocity signal at $x/x_T = 1$, $y = 0$). It is usually made nondimensional as $f_j b/U_c$

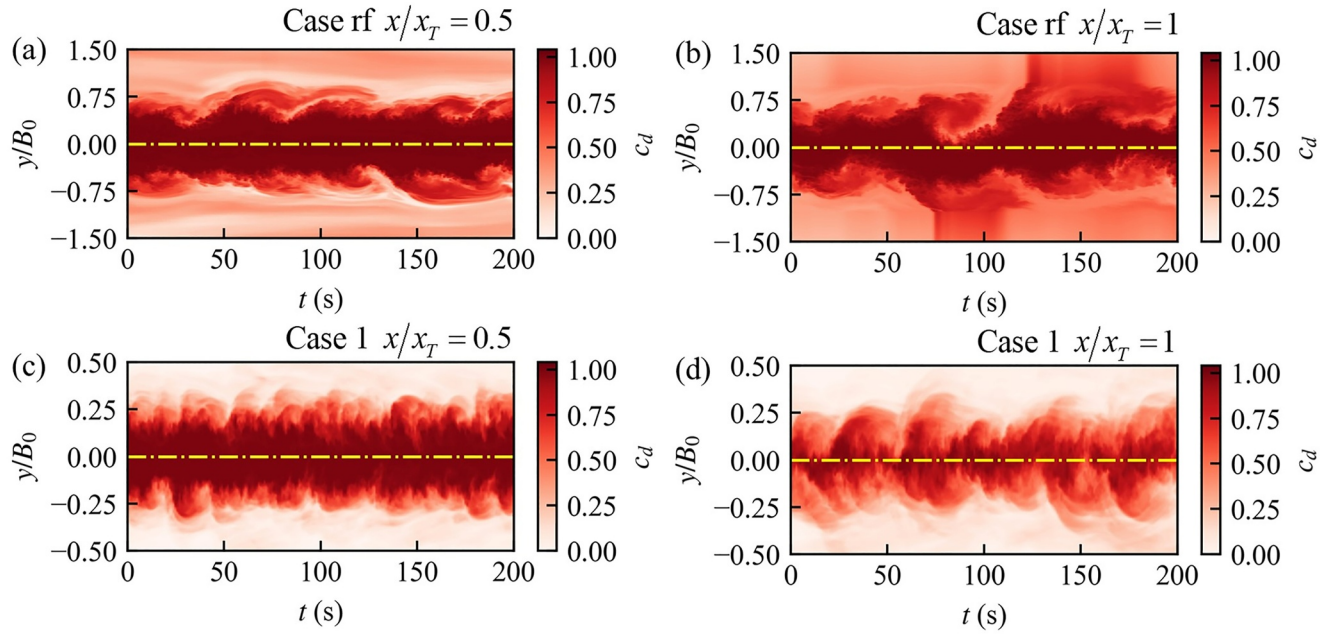

Figure 16. Time series of depth-averaged instantaneous concentration c_d at $x/x_T = 0.5$ (left panels) and $x/x_T = 1$ (right panels) for Case rf (top panels) and Case 1 (bottom panels). Colorbars: concentration range. Yellow dash-dotted lines represent the centerline: $y/B_0 = 0$.

(Jirka, 2001) or $f_j B_0/U_0$ (Cohen, 2012; Deo et al., 2007), and ranges between 0.08 and 0.5 (Cohen, 2012). The numerical results gave $f_j b/U_c \sim 0.3$ for both Case 1 and Case rf, within the range reported in the literature. The jet flapping motion also brings ambient water to the centerline (Figure 16d), resulting in a decreased depth-averaged concentration at ($x/x_T = 1$, $y = 0$) in Case 1 (equal to 0.86 after time-averaging). In contrast, the jet flapping motion in Case rf is not strong enough to influence the centerline concentration, and at ($x/x_T = 1$, $y = 0$), the time-averaged concentration is still equal to unity. The stronger jet-flapping in Case 1 also produces a region ($0.75 < x/x_T < 1$) with strong momentum exchange (Figures 9a and 9b); this is much less evident in Case rf (Figure 9c). Previous studies pointed out that the instability of a jet is related to aspect ratio b/H and bottom friction (Canestrelli et al., 2014; Jirka, 1994; Socolofsky & Jirka, 2004): that is, the strength of the jet flapping motion is expected to be stronger with a smaller aspect ratio and smaller bottom friction. The main difference between Case 1 and Case rf is the aspect ratio at $x/x_T = 1$, which is only $b/h_c = 1.3$ in Case 1, but can be as large as $b/h_c = 37.5$ in Case rf.

3.6. Application of the Numerical Model to Other Slopes

To determine the effect of the bottom slope angle on jet characteristics, the numerical model was applied to jets flowing over three additional slopes: $\beta = 1°$, 2°, and 4° under the same inflow conditions as Case 1 and Case rf (Table 1). Increase of jet thickness, which is controlled by bottom slope (Figure 17a), leads to nearshore contraction of the jet (Figure 17b), even with a slope angle as small as 1°. A larger bottom slope leads to a more rapid thickness increase and width decrease in the flow establishment zone. As a result, the length of the flow establishment zone (x_T) decreases with increasing bottom slope (Figure 17c). For the 2° sloping bottom, the numerical model gives ($x_T/B_0 \approx 2.4$), which is close to the value obtained from Figure 2 in the coastal environment ($x_T/B_0 \approx 2.7$), suggesting that the outflow from a channel or an outlet in the coastal environment can be well characterized by a plane jet over a sloping bottom. The time and depth-averaged centerline concentration ($\overline{c}_d$) at $x/x_T = 1$ also decreases with an increase of the bottom slope angle (Figure 17c). This indicates that the strength of the jet-flapping motion increases with an increasing bottom slope angle due to a smaller aspect ratio (b/h_c) at $x/x_T = 1$ (Figures 17a and 17b). With an increasing slope angle, the rate of change of the depth-averaged centerline velocity increases rapidly in the nearshore zone as shown in Figure 17d. These results emphasize the sensitivity of the mean flow parameters to the slope angle in the flow establishment zone, even for small slope angles. The detailed study of the flow over an 8° slope presented in the previous sections shows that the change in all the other hydrodynamic characteristics (compared to the horizontal bottom case) is related to the mean flow parameters

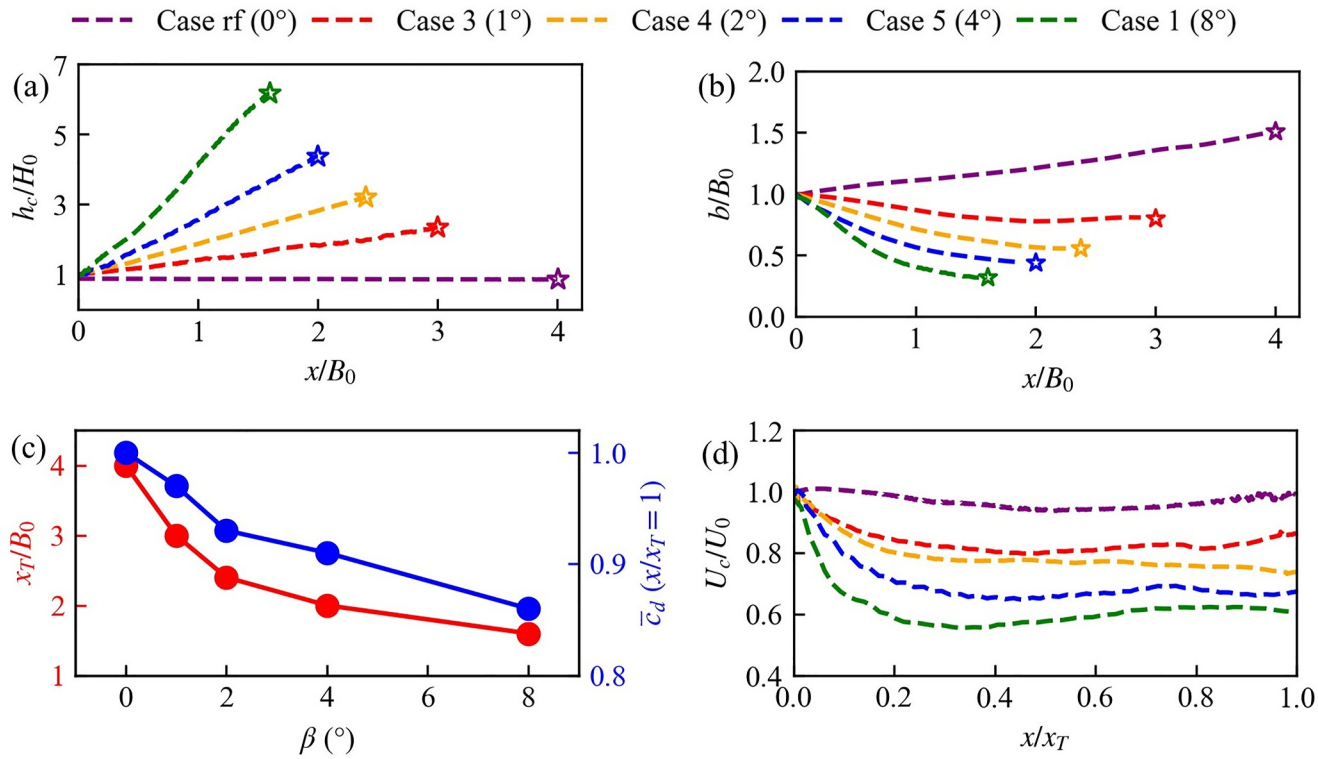

Figure 17. Variations of (a) jet thickness, (b) width in the flow establishment zone for numerical cases with different bottom slopes. Stars mark the end of this zone (x_T). (c) Comparison of x_T (red; left vertical axis) and time and depth-averaged centerline concentration at $x/x_T = 1$ (blue; right vertical axis) for cases with different bottom slopes. (d) Variations of the depth-averaged centerline velocity in the flow establishment zone in numerical cases with different bottom slopes. The x coordinate is nondimensionalized by x_T which is different from the nondimensionalization in (a) and (b). Colors in (a), (b), (d) are defined by the top legends.

discussed in this section. Therefore, it can be assumed that the remaining jet characteristics (i.e., development of shear layers, vertical extension of KHCS and jet flapping motion strength) also change with slope angle.

3.7. Summary of Similarities and Differences Between Sloping Bottom and Horizontal Bottom Jets

Comparing the results of the present study for a jet flowing over a sloping bottom with the quasi-2D plane jet over a horizontal bottom, the following similarities and differences in terms of mean flow field and turbulence characteristics (Section 3.7.1) and Kelvin Helmholtz-type coherent structures (Section 3.7.2) were found.

3.7.1. Mean Field Development and Turbulence Characteristics

Similarities:

- In the nearfield, the transverse profile of the longitudinal jet velocity transforms from a "top-hat" shaped profile (flow establishment zone) into a Gaussian distribution (established flow zone).
- Shear layers develop and grow on both sides of the jet due to the presence of the velocity gradient between the jet and ambient water.
- Strong signals of turbulent kinetic energy are observed in the shear layers.

Differences:

- The jet over a sloping bottom spreads vertically. Under the combined influence of the vertical spreading and lateral entrainment, the jet contracts before spreading laterally as seen in observations in the coastal environment (Figure 2).
- For the 8° sloping bottom jet, the transition to the Gaussian distribution occurs at $x_T \approx 1.6B_0$, which is 0.4 times that of the horizontal bottom jet ($x_T \approx 4B_0$). Thus, the length of the flow establishment zone is significantly

reduced. Results of the analysis for different slope angles show that the length of the flow establishment is sensitive to the slope angle.

- The centerline velocity decreases near the channel mouth in sloping bottom jets but remains constant in the horizontal bottom jet in the flow establishment zone.
- The momentum thickness of the shear layers increases with distance in the flow establishment zone and then remains almost constant thereafter in the 8° sloping bottom case. In the horizontal bottom case, however, the momentum thickness continuously increases in the flow establishment zone and in the established flow zone.

3.7.2. Kelvin Helmholtz-Type Coherent Structures

Similarities:

- In the shear layers, Kelvin Helmholtz-type Coherent Structures (KHCS) are generated, whose horizontal size increases with increasing offshore distance. This agrees with observations in the coastal environment (Figure 2).
- KHCS result in quasi-periodic velocity fluctuations at the interface between the jet and ambient water. A nearly constant Strouhal number of ∼0.079 is observed for these KHCS.
- Jet flapping occurs after the shear layers merge at the centerline (at around $x/x_T = 1$).

Differences:

- The vertical size of KHCS in the 8° sloping bottom jet increases with increasing distance from the channel mouth because of the vertical spreading of the jet.
- The jet-flapping motion is strong enough to influence the centerline concentration in sloping bottom jets at $x/x_T = 1$, whereas it is not for the jet over the horizontal bottom.

4. Conclusion

This paper presents the first laboratory study that documents the evolution of an initially shallow, neutrally buoyant jet, bounded by an 8° sloping, solid bottom boundary and an upper free surface, that issues into a laterally unconfined, quiescent ambient. Such jet flow occurs in coastal environments when a body of water discharges into an ocean or a lake through a channel or an outlet. A 3D numerical model using Large Eddy Simulation (LES) was developed and validated with the experimental data. Our experimental and numerical results indicate that existing analytical models for plane jets over sloping bottoms underestimate the jet width and overestimate the centerline velocity. Furthermore, a comparison was made with a plane jet flowing over a horizontal bottom with the same flow conditions. Our study has demonstrated that unlike the horizontal bottom jet which behaves like a quasi-2D plane jet, the flow field of the sloping bottom jet is clearly 3D.

Vertical spreading of the sloping bottom jet causes a horizontal contraction in the nearshore region and a smaller x_T, which means a narrower and shorter flow establishment zone than a quasi-2D horizontal bottom jet. This difference is important when evaluating the effective domain of a jet flow, especially when estimating the transport of materials (e.g., sediment, pollution, nutrients, fish larvae) by the jet. A sloping bottom also results in a decrease of centerline velocity near the channel mouth that has not been considered by existing analytical models. This behavior may cause deposition of large-sized suspended sediment and thus influence the evolution of nearshore geomorphology.

Kelvin Helmholtz-type Coherent Structures developing in shear layers on both sides of the jet are found to be the main contributor to momentum exchange and the production of turbulent kinetic energy. KHCS meet at the centerline after a certain distance ($x/x_T = 1$) and cause the entire jet to flap. In sloping bottom jets, the jet-flapping motion is strong enough to influence the centerline concentration at $x/x_T = 1$, which further decreases with increasing sloping bottom angle. These large-scale turbulent structures (KHCS and jet flapping) have a considerable impact on momentum exchange and energy production. Consequently, it is necessary to use a 3D model that can capture these structures when studying jet hydrodynamics. The LES-based model applied in the present study allowed reproduction of 3D details of jet flows that are not fully accessible in experimental studies and field measurements.

Although a simplified geometry with a uniform bottom slope was applied in this study, the present numerical model can be applied to more complex coastal geometries shaped by jet erosion and ebb delta deposit in future studies. It

also has the potential to be extended to simulate sediment behavior (deposition and erosion) in jet flows in the coastal environment, as well as to study the evolution of nearshore geomorphology. These features are important since they affect the environmental impact of discharge from a channel or an outlet into a coastal environment.

Supporting Information

The Supporting Information file contains more detailed information on the experiments, numerical modeling and quadrant analysis.

Data Availability Statement

Data reported in this paper can be downloaded from the open-access repository in Shi et al. (2024).

Acknowledgments
The authors are indebted to S. Viboud and T. Valran for their support in conducting the experiments at the Coriolis Platform at LEGI (Université Grenoble Alpes, CNRS, Grenoble, France) and are grateful to E. J. Hopfinger for his suggestions. We would like to thank the anonymous reviewers for the constructive comments and suggestions.

References

Antonia, R. A., Browne, L. W. B., Rajagopalan, S., & Chambers, A. J. (1983). On the organized motion of a turbulent plane jet. *Journal of Fluid Mechanics*, *134*(1), 49–66. https://doi.org/10.1017/S0022112083003213

Athanasiou, P., van Dongeren, A., Giardino, A., Vousdoukas, M., Gaytan-Aguilar, S., & Ranasinghe, R. (2019). Global distribution of nearshore slopes with implications for coastal retreat. *Earth System Science Data*, *11*(4), 1515–1529. https://doi.org/10.5194/essd-11-1515-2019

Bagherimiyab, F., & Lemmin, U. (2018). Large-scale coherent flow structures in rough-bed open-channel flow observed in fluctuations of three-dimensional velocity, skin friction and bed pressure. *Journal of Hydraulic Research*, *56*(6), 806–824. https://doi.org/10.1080/00221686.2017.1416686

Bianchi, T. S., & Allison, M. A. (2009). Large-river delta-front estuaries as natural "recorders" of global environmental change. *Proceedings of the National Academy of Sciences of the United States of America*, *106*(20), 8085–8092. https://doi.org/10.1073/pnas.0812878106

Broekema, Y. B., Labeur, R. J., & Uijttewaal, W. S. J. (2018). Observations and analysis of the horizontal structure of a tidal jet at deep scour holes. *Journal of Geophysical Research: Earth Surface*, *123*(12), 3162–3189. https://doi.org/10.1029/2018JF004754

Brown, C. A., Jackson, G. A., & Brooks, D. A. (2000). Particle transport through a narrow tidal inlet due to tidal forcing and implications for larval transport. *Journal of Geophysical Research*, *105*(C10), 24141–24156. https://doi.org/10.1029/2000JC000211

Brown, G. L., & Roshko, A. (1974). On density effects and large structure in turbulent mixing layers. *Journal of Fluid Mechanics*, *64*(4), 775–816. https://doi.org/10.1017/S002211207400190X

Canestrelli, A., Nardin, W., Edmonds, D., Fagherazzi, S., & Slingerland, R. (2014). Importance of frictional effects and jet instability on the morphodynamics of river mouth bars and levees. *Journal of Geophysical Research: Oceans*, *119*(1), 509–522. https://doi.org/10.1002/2013JC009312

Cohen, C. (2012). Shallow-water plane and tidal jets. Unpublished Ph.D. thesis. University of Otago. Retrieved from https://ourarchive.otago.ac.nz/handle/10523/2493

De Lorenzis, L., & Düster, A. (2020). *Modeling in engineering using innovative numerical methods for solids and fluids* (Vol. 599). CISM International Centre for Mechanical Sciences, Springer International Publishing. https://doi.org/10.1007/978-3-030-37518-8

Deo, R. C., Mi, J., & Nathan, G. J. (2007). The influence of nozzle-exit geometric profile on statistical properties of a turbulent plane jet. *Experimental Thermal and Fluid Science*, *32*(2), 545–559. https://doi.org/10.1016/j.expthermflusci.2007.06.004

Deo, R. C., Mi, J., & Nathan, G. J. (2008). The influence of Reynolds number on a plane jet. *Physics of Fluids*, *20*(7), 075108. https://doi.org/10.1063/1.2959171

Dimotakis, P. E. (1991). Turbulent free shear layer mixing and combustion. In *High speed flight propulsion systems* (pp. 265–340). American Institute of Aeronautics and Astronautics. https://doi.org/10.2514/4.866104

Dracos, T., Giger, M., & Jirka, G. H. (1992). Plane turbulent jets in a bounded fluid layer. *Journal of Fluid Mechanics*, *241*, 587–614. https://doi.org/10.1017/S0022112092002167

Geyer, W. R., Lavery, A. C., Scully, M. E., & Trowbridge, J. H. (2010). Mixing by shear instability at high Reynolds number. *Geophysical Research Letters*, *37*(22), 2010GL045272. https://doi.org/10.1029/2010GL045272

Giger, M., Dracos, T., & Jirka, G. H. (1991). Entrainment and mixing in plane turbulent jets in shallow water. *Journal of Hydraulic Research*, *29*(5), 615–642. https://doi.org/10.1080/00221689109498980

Heskestad, G. (1965). Hot-wire measurements in a plane turbulent jet. *Journal of Applied Mechanics*, *32*(4), 721–734. https://doi.org/10.1115/1.3627309

Ho, C. M., & Huang, L. S. (1982). Subharmonics and vortex merging in mixing layers. *Journal of Fluid Mechanics*, *119*, 443–473. https://doi.org/10.1017/S0022112082001438

Ho, C. M., & Huerre, P. (1984). Perturbed free shear layers. *Annual Review of Fluid Mechanics*, *16*(1), 365–422. https://doi.org/10.1146/annurev.fl.16.010184.002053

Huai, W. X., Zhang, J., Wang, W. J., & Katul, G. G. (2019). Turbulence structure in open channel flow with partially covered artificial emergent vegetation. *Journal of Hydrology*, *573*, 180–193. https://doi.org/10.1016/j.jhydrol.2019.03.071

Jasak, H. (2009). OpenFOAM: Open source CFD in research and industry. *International Journal of Naval Architecture and Ocean Engineering*, *1*(2), 89–94. https://doi.org/10.2478/IJNAOE-2013-0011

Jiménez-Robles, A. M., Ortega-Sánchez, M., & Losada, M. A. (2016). Effects of basin bottom slope on jet hydrodynamics and river mouth bar formation. *Journal of Geophysical Research: Earth Surface*, *121*(6), 1110–1133. https://doi.org/10.1002/2016JF003871

Jirka, G. H. (1994). Shallow jets. In P. A. Davies, & M. J. V. Neves (Eds.), *Recent research advances in the fluid mechanics of turbulent jets and plumes* (Vol. 255, pp. 157–175). Springer. https://doi.org/10.1007/978-94-011-0918-5_10

Jirka, G. H. (2001). Large scale flow structures and mixing processes in shallow flows. *Journal of Hydraulic Research*, *39*(6), 567–573. https://doi.org/10.1080/00221686.2001.9628285

Landel, J. R., Caulfield, C. P., & Woods, A. W. (2012). Meandering due to large eddies and the statistically self-similar dynamics of quasi-two-dimensional jets. *Journal of Fluid Mechanics*, *692*, 347–368. https://doi.org/10.1017/jfm.2011.518

Lee, H., & Yu, W. (1997). Experimental study of reservoir turbidity current. *Journal of Hydraulic Engineering*, *123*(6), 520–528. https://doi.org/10.1061/(ASCE)0733-9429(1997)123:6(520)

Li, D., Liu, M., & Huai, W. (2022). Modeling transverse momentum exchange in partially vegetated flow. *Physics of Fluids*, *34*(2), 025124. https://doi.org/10.1063/5.0081202

McKee, B. A., Aller, R. C., Allison, M. A., Bianchi, T. S., & Kineke, G. C. (2004). Transport and transformation of dissolved and particulate materials on continental margins influenced by major rivers: Benthic boundary layer and seabed processes. *Continental Shelf Research*, *24*(7–8), 899–926. https://doi.org/10.1016/j.csr.2004.02.009

Nezu, I., & Nakagawa, H. (1993). *Turbulence in open-channel flows*. IAHR. https://doi.org/10.1201/9780203734902

Odier, P., Chen, J., & Ecke, R. E. (2012). Understanding and modeling turbulent fluxes and entrainment in a gravity current. *Physica D: Nonlinear Phenomena*, *241*(3), 260–268. https://doi.org/10.1016/j.physd.2011.07.010

Oler, J. W., & Goldschmidt, V. W. (1982). A vortex-street model of the flow in the similarity region of a two-dimensional free turbulent jet. *Journal of Fluid Mechanics*, *123*, 523–535. https://doi.org/10.1017/S0022112082003188

Onishi, S. (1984). Study of vortex structure in water surface jets by means of remote sensing. *Elsevier Oceanography Series*, *38*, 107–132. https://doi.org/10.1016/S0422-9894(08)70607-X

Ortega-Sánchez, M., Losada, M. A., & Baquerizo, A. (2008). A global model of a tidal jet including the effects of friction and bottom slope. *Journal of Hydraulic Research*, *46*(1), 80–86. https://doi.org/10.1080/00221686.2008.9521845

Özsoy, E., & Ünlüata, Ü. (1982). Ebb-tidal flow characteristics near inlets. *Estuarine, Coastal and Shelf Science*, *14*(3), 251–263. https://doi.org/10.1016/S0302-3524(82)80015-7

Panchapakesan, N. R., & Lumley, J. L. (1993). Turbulence measurements in axisymmetric jets of air and helium. Part 1. Air jet. *Journal of Fluid Mechanics*, *246*, 197–223. https://doi.org/10.1017/S0022112093000096

Pope, S. B. (2000). *Turbulent flows*. Cambridge University Press. https://doi.org/10.1017/CBO9780511840531

Rogers, M. M., & Moser, R. D. (1992). The three-dimensional evolution of a plane mixing layer: The Kelvin–Helmholtz rollup. *Journal of Fluid Mechanics*, *243*(1), 183–226. https://doi.org/10.1017/S0022112092002696

Rowland, J. C., Stacey, M. T., & Dietrich, W. E. (2009). Turbulent characteristics of a shallow wall-bounded plane jet: Experimental implications for river mouth hydrodynamics. *Journal of Fluid Mechanics*, *627*, 423–449. https://doi.org/10.1017/S0022112009006107

Shaw, W. J., & Trowbridge, J. H. (2001). The direct estimation of near-bottom turbulent fluxes in the presence of energetic wave motions. *Journal of Atmospheric and Oceanic Technology*, *18*(9), 1540–1557. https://doi.org/10.1175/1520-0426(2001)018<1540:TDEONB>2.0.CO;2

Shi, H., Negretti, M. E., Chauchat, J., Blanckaert, K., Lemmin, U., & Barry, D. A. (2022). Unconfined plunging of a hyperpycnal river plume over a sloping bed and its lateral spreading: Laboratory experiments and numerical modeling. *Water Resources Research*, *58*(8), e2022WR03263. https://doi.org/10.1029/2022WR032633

Shi, H., Negretti, M. E., Chauchat, J., Blanckaert, K., Lemmin, U., & Barry, D. A. (2024). Data set for "Tracking the nearfield evolution of an initially shallow, neutrally-buoyant plane jet over a sloping bottom boundary" [Dataset]. *Zenodo*. https://doi.org/10.5281/zenodo.10466800

Shi, H., Zhang, J., & Huai, W. (2023). Experimental study on velocity distributions, secondary currents, and coherent structures in open channel flow with submerged riparian vegetation. *Advances in Water Resources*, *173*, 104406. https://doi.org/10.1016/j.advwatres.2023.104406

Shih, T. H., Liou, W. W., Shabbir, A., Yang, Z., & Zhu, J. (1995). A new k-ϵ eddy viscosity model for high Reynolds number turbulent flows. *Computers & Fluids*, *24*(3), 227–238. https://doi.org/10.1016/0045-7930(94)00032-T

Shiono, K., & Knight, D. W. (1991). Turbulent open-channel flows with variable depth across the channel. *Journal of Fluid Mechanics*, *222*(1), 617–646. https://doi.org/10.1017/S0022112091001246

Siebert, H., Lehmann, K., & Wendisch, M. (2006). Observations of small-scale turbulence and energy dissipation rates in the cloudy boundary layer. *Journal of the Atmospheric Sciences*, *63*(5), 1451–1466. https://doi.org/10.1175/JAS3687.1

Socolofsky, S. A., & Jirka, G. H. (2004). Large-scale flow structures and stability in shallow flows. *Journal of Environmental Engineering and Science*, *3*(5), 451–462. https://doi.org/10.1139/s04-032

Taborda, C., Fael, C., Ricardo, A. M., & Ferreira, R. M. L. (2022). Wave-like motion and secondary currents in arrays of emergent cylinders induced by large scale eddying motion. *Environmental Fluid Mechanics*, *22*(2–3), 403–428. https://doi.org/10.1007/s10652-022-09863-4

Thomas, F. O., & Goldschmidt, V. W. (1986). Structural characteristics of a developing turbulent planar jet. *Journal of Fluid Mechanics*, *163*, 227–256. https://doi.org/10.1017/S0022112086002288

Truong, S. H., & Uijttewaal, W. S. J. (2019). Transverse momentum exchange induced by large coherent structures in a vegetated compound channel. *Water Resources Research*, *55*(1), 589–612. https://doi.org/10.1029/2018WR023273

Weller, H. G., Tabor, G., Jasak, H., & Fureby, C. (1998). A tensorial approach to computational continuum mechanics using object-oriented techniques. *Computers in Physics*, *12*(6), 620–631. https://doi.org/10.1063/1.168744

White, B. L., & Nepf, H. M. (2008). A vortex-based model of velocity and shear stress in a partially vegetated shallow channel. *Water Resources Research*, *44*(1), W01412. https://doi.org/10.1029/2006WR005651

Yao, H. Y., Leonardi, N., Li, J. F., & Fagherazzi, S. (2016). Sediment transport in a surface-advected estuarine plume. *Continental Shelf Research*, *116*, 122–135. https://doi.org/10.1016/j.csr.2016.01.014

Yuan, Y., & Horner-Devine, A. R. (2017). Experimental investigation of large-scale vortices in a freely spreading gravity current. *Physics of Fluids*, *29*(10), 106603. https://doi.org/10.1063/1.5006176

References From the Supporting Information

Cowen, E. A., & Monismith, S. G. (1997). A hybrid digital particle tracking velocimetry technique. *Experiments in Fluids*, *22*(3), 199–211. https://doi.org/10.1007/s003480050038

Kim, W. W., & Menon, S. (1995). A new dynamic one-equation subgrid-scale model for large eddy simulations. In *33rd aerospace sciences meeting and exhibit*. https://doi.org/10.2514/6.1995-356

Ooi, S. K., Constantinescu, G., & Weber, L. (2009). Numerical simulations of lock-exchange compositional gravity current. *Journal of Fluid Mechanics*, *635*, 361–388. https://doi.org/10.1017/S0022112009007599

Prasad, A. K., Adrian, R. J., Landreth, C. C., & Offutt, P. W. (1992). Effect of resolution on the speed and accuracy of particle image velocimetry interrogation. *Experiments in Fluids*, *13*(2–3), 105–116. https://doi.org/10.1007/BF00218156

Roache, P. J. (1994). Perspective: A method for uniform reporting of grid refinement studies. *Journal of Fluids Engineering*, *116*(3), 405–413. https://doi.org/10.1115/1.2910291

Roache, P. J. (1997). Quantification of uncertainty in computational fluid dynamics. *Annual Review of Fluid Mechanics*, *29*(1), 123–160. https://doi.org/10.1146/annurev.fluid.29.1.123

Tominaga, Y., & Stathopoulos, T. (2007). Turbulent Schmidt numbers for CFD analysis with various types of flow field. *Atmospheric Environment*, *41*(37), 8091–8099. https://doi.org/10.1016/j.atmosenv.2007.06.054